The Pennsylvania State University

The Graduate School

College of Engineering

ICE PROJECTILE LENGTH PREDICTION OF SHED ICE FROM

ROTOR BLADES

A Thesis in

Aerospace Engineering

by

Grant M. Schneeberger

Submitted in Partial Fulfillment

of the Requirements

for the Degree of

Master of Science

December 2016

The thesis of Grant M. Schneeberger was reviewed and approved* by the following:

Jose L. Palacios

Assistant Professor of Aerospace Engineering

Thesis Advisor

Richard R. Auhl

Aerospace Engineering Laboratory Director

Philip J. Morris

Professor of Aerospace Engineering

Interim Head of the Department of Aerospace Engineering

*Signatures are on file in the Graduate School.

Abstract

Ice shed from rotor blades can be a ballistic concern for conventional helicopters, tiltrotors, wind turbines, and propellers. In conventional helicopters these ice projectiles can cause damage to the empennage and tail rotor, and in a tiltrotor configuration fuselage damage can be a concern. In both types of rotorcraft the ice could be ingested by the engine. All of these can lead to a catastrophic failure of the rotorcraft. A significant amount of research has already been conducted on adhesion strength of ice, ice shedding, projectile trajectories, and impact damage. This thesis will discuss research conducted to predict the ice projectile length of shed ice leaving the tip of a rotating blade. Knowing the size of the ice projectile is critical during the design of ice protection systems and critical structures that could be impacted by shed ice.

Two models (based on Euler-Bernoulli and Timoshenko beam theories respectively) were developed to predict the length of shed ice as it slides past the tip of the rotor blade due to the effect of centrifugal force. The failure mechanism of the ice was determined to be due to direct stresses created by the bending of the ice shape as it hangs over the rotor blade tip. These direct stresses exceeded the ultimate strength of the ice once the overhanging ice structure reached a critical

length. An Euler-Bernoulli model for ultimate tensile strength failure was compared to a Timoshenko shear failure model. Comparison of the models confirmed failure due to direct tensile stress.

Given the large discrepancy of the reported values of ultimate tensile strength of ice found in literature, this value was experimentally measured in this research for impact ice shapes. The Pennsylvania State University's Adverse Environment Rotor Test Stand (AERTS) was used to create ice at representative in-flight icing conditions. Such ice shapes were removed from the rotor and used to determine the tensile strength of impact ice. The ultimate tensile strength of impact ice was found to be 0.685 MPa with a relative standard deviation of 38%.

The same facility was used to conduct experiments to visualize ice sliding down the rotor blade upon shedding and the breaking up of the ice projectiles was quantified during rotation. The cross-section of the ice shapes was photographed prior to inducing shedding. These ice shape were then digitized and the second moments of area and centroid were found for the accreted ice shapes. Electro-thermal heaters were used to induce the accreted ice to shed during rotation and high-speed cameras were used to capture the breakup of ice as it traveled over the tip of the rotor. Quantification of the break lengths of the ice projectiles was obtained. Using the measured cross-sectional properties of the shed ice cross-sections and the ultimate tensile strength of ice experimentally quantified, the model was able to predict the break length within 11% of the experimentally measured lengths for the entire data set. Knowledge of the cross-sectional properties closer to the fracture face of the ice projectile results in predictions within 8.6% of the experimentally measured lengths as compared to 13% for cross-sectional properties estimated using

the ice shape at the tip of the rotor blade.

Table of Contents

List of Figures

List of Tables

List of Symbols

ρ Density of Air at -14°C $\left(\frac{kg}{m^3}\right)$

v   Tip Speed of Rotor Blade $\left(\frac{m}{sec}\right)$

C_d Section Drag Coefficient $(non-dimensional)$

chord   Chord of Ice Beam (mm)

R   Blade Radius (m)

Ω Rotational Speed of Rotor Shaft$\left(\frac{rad}{sec}\right)$

l   Ice Length (cm)

M   Bending Moment at Ice Beam Root $(N-m)$

c   Distance from centroid of Ice Beam to the Leading Edge (m)

I   Second Area Moment of Intertia (m^4)

drag   Drag Force (N)

ϕ Rotation of the Ice Beam Cross-Section $(non-dimensional)$

G   Modulus of Rigidty (Pa)

k   shear correction factor $(non-dimensional)$

w_0 transverse deflection of the Ice Beam (m)

EI   Flexural Rigidity (Nm^2)

A   Ice Shape Cross Sectional Area (m^2)

q_0 Uniform Distributed Load $(\frac{N}{m})$

$\bar{M}_x$ Effective Bending Moment about the x-axis (Nm)

$\bar{M}_y$ Effective Bending Moment about the y-axis (Nm)

I_{xx} Second Moment of Area about the x-axis (m^4)

I_{yy} Second Moment of Area about the y-axis (m^4)

I_{xy} Second Moment of Area about the xy-plane (m^4)

$\bar{y}$ y Distance From Centroid to Location of Maximum Tensile Stress (m)

$\bar{x}$ x Distance From Centroid to Location of Maximum Tensile Stress (m)

Acknowledgments

I would like to sincerely thank my advisor and mentor, Dr. Palacios, for his commitment, guidance, and time invested into my research. I also owe a great deal of thanks to one of my fellow graduate students, Jared Solitis. Jared's contributions and expertise were indispensable throughout the entire process of completing this thesis. My research would not have been a success without the help of these two people. I would like to thank both Richard Auhl and Dr. McLaughlin for not only encouraging me to return to school and completing a Masters degree, but also for serving as my temporary advisors before I transitioned to Dr. Palacios' team.

I owe a great deal of gratitude to my fellow graduate students and colleagues, Ahmad Haidar, Ed Rocco, Sihong Yan, Yiqiang Han, Belen Veras-Alba, Miguel Alvarez, Bryce Connelly, and Tirth Patel. I can't thank all of you enough for the time and recommendations you provided as well as the supportive environment you helped to create.

Last, but certainly not least, I am eternally grateful for the love and support of my parents, Noel and Libby Schneeberger. I can't thank you enough for your words of wisdom and encouragement throughout my academic career. I could not be where I am today without you.

Chapter 1

Introduction

1.1 Overview of Icing Research

1.1.1 General Icing Research History

At the inception of powered flight, aviators were not concerned with aircraft icing and the problems it would pose. These early pilots lacked instruments which were crucial for flying without having visual references and therefore, did their best to steer clear of clouds. This began to change in the mid-1920s with the arrival of flight instrumentation such as gyroscopic turn indicators, ball-bank indicators, and airspeed indicators. Using these new instruments, pilots began to adopt Instrument Flight Rules (IFR) and fly in conditions where there were not any visual references. The pilots of the U.S. Air Mail Service's New York and Chicago route became the first group of aviators to face icing challenges on a regular basis. These pilots believed that icing was the greatest hazard of their flights [8].

In 1928, in response to a growing aviation industry where icing was becoming a much larger problem, the National Advisory Council for Aeronautics (NACA) constructed the first refrigerated icing wind tunnel at Langley. The facility was

constructed out of an insulated metal shell, a commercial refrigeration system for cooling, a propeller to circulate the air, and four commercial spray nozzles. By controlling water pressure and air pressure to the nozzles, an artificial cloud could be created. There were two major drawbacks to this facility. First, the test section was only 6 inches in diameter, which seriously limited the size of models that could be tested. Second, the commercial nozzles used were not capable of producing small enough water droplets to recreate natural icing conditions. Despite the drawbacks icing research was possible, but it became clear that a more robust facility was necessary [8].

In the spring of 1942, the NACA began the design and construction of the Icing Research Tunnel (IRT) in Cleveland, Ohio. The IRT was part of a much larger facility, formerly known as the Aircraft Engine Research Laboratory (now known as NASA Glenn). The IRT had a test section that was 6 ft by 9 ft by 25 ft, a significant improvement over the facility in Langley. In August of 1944, the first experiments had been performed on bare-blade propeller icing in the new tunnel [8].

Since construction of the IRT in 1942, several privately owned tunnels have been constructed. Some of the larger facilities include the Goodrich Icing Wind Tunnel constructed in 1988 in Uniontown, Oh [9], the Boeing Research Aerodynamic Icing Tunnel (BRAIT) constructed in 1991 outside of Seattle, WA [10], and the Cox Icing Wind Tunnel constructed in 1995 in Manhattan, NY [11]. There have also been facilities designed to perform full scale helicopter icing research. Some of these facilities include the Helicopter Icing Spray System (HISS) [12] and the McKinley Climatic Laboratory [13]. In 2009, The Pennsylvania State University introduced the Adverse Environment Rotor Test Stand (AERTS). AERTS is a unique facility that features a hover stand designed for icing testing of small-scale (3m diameter) rotor blades [14]. Testing is not only limited to helicopter scaled rotors, but also

wind turbine blades and propeller configurations.

1.1.2 Rotor Blade Icing History

Due to the complexity of vertical lift, research and technology on rotary-wing aircraft lagged behind that of fixed wing. In 1970s, there was a significant amount of interest in rotorcraft icing research. The interest was driven by new design requirements and the opportunities new technology presented. At the time, both the military and commercial companies had a similar need for helicopters. The military needed helicopters that were capable of operating throughout Europe during the winter, and commercial companies needed helicopters that were capable of servicing oil rigs off the Alaskan coast and in the North Sea [8].

Researchers began to look at de-icing systems that worked for fixed wing applications and tried to apply them to rotorcraft. Under an army contract in the 1970's, Lockheed Aircraft began exploring an improved version of the Goodrich de-icer boot, a simple pneumatic device. The boot was originally designed using neoprene rubber. This material was unable to withstand heavy rain and centrifugal forces and the concept was rejected. Goodrich went back to the drawing board and investigated multiple materials to improve the boots durability. They determined that polyurethane would solve the problem and in 1979, with NASA's help, they tested the boot. Testing determined the improved boot was a feasible rotor protection system [8].

In the 1980s, NASA spent a great deal of time investigating Electro-Impulse De-Icing (EIDI) systems. While these systems proved promising, they never lived up to the hype. In the mid 1980's, research efforts shifted towards a more fundamental understanding of the physics behind icing and ways to model ice accretion on

airfoils. This led to NASA developing a standard model for icing predictions known as LEWICE [8].

1.2 Rotor Blade Icing Physics

A rotorcraft is subject to in flight icing when it is operating at temperatures below 0°C and is flying through an icing cloud. Despite being called an icing cloud there are no ice particles in the cloud. These clouds contain super-cooled (<0°C) liquid water droplets. As the rotorcraft flies through the cloud, the super-cooled water droplets freeze completely or partially immediately upon impact with the surface of the rotor. The percentage of the droplet that freezes on impact is dependent upon a balance of thermodynamic processes referred to as the freezing fraction [15].

1.2.1 Ice Accretion

Ice accretion is the buildup of an ice deposit on the leading edge of rotor blades. The rate of accretion and the shape the deposit of ice takes on is dependent upon airspeed and a number of atmospheric conditions in icing cloud. These atmospheric conditions are air temperature, water droplet size, amount of water in the cloud, and the time spent flying through the cloud at the above conditions.

The air temperature will determine if the super-cooled water particles freeze immediately or partially upon impact. This affects the shape of ice accreted. The water droplets in a cloud are never all the same size. For this reason, the parameter is defined by the median volumetric diameter (MVD) of the water particles in the cloud and is measured in μm. The amount of water in the cloud is defined as liquid water content (LWC), which is simply the density of water in the cloud, measured

in g/m^3. The higher the LWC the greater the rate of accretion.

The three parameters described above (ambient temperature, LWC, and MVD) are used to parameterize the icing envelope as defined by the Federal Aviation Administration (FAA). The FAA defines two icing envelopes, continuous and intermittent, in the Federal Aviation Regulations Part 25 and 29 Appendix C for aircraft and rotorcraft respectively. The continuous icing envelope is shown in Figure 1.1 and represents icing conditions seen by a vehicle which are less severe. In this envelope LWC is low and ranges from 0.06 to 0.8 g/m^3. The intermittent icing envelope is also shown in Figure 1.1 and represents extreme icing conditions. In this envelope LWC is high and ranges from 0.3 to 2.9 g/m^3. Typically these icing conditions are only experienced for a short period of time. All artificial icing test facilities must use these icing envelopes in order to create conditions representative of natural icing [1].
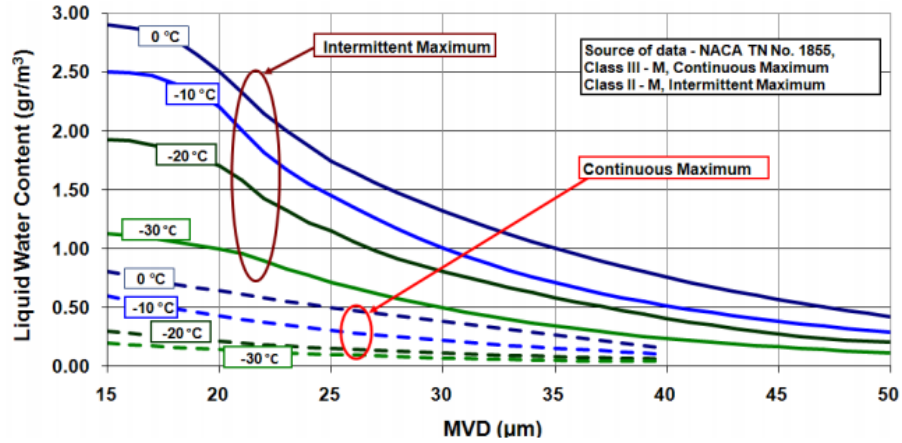
Figure 1.1. Federal Aviation Regulations Icing Envelopes [1]

5

1.2.2 Ice Shapes

Accreted ice can be categorized into three regimes, glaze, mixed, and rime. Each of these regimes will take on a unique general shape and determining which regime will accrete is not simple. The regime of ice produced is dependent upon the freezing fraction, which in turn depends on the ambient temperature, LWC of the cloud, and MVD of the water particles. In general it is much easier to determine the ice regime after the ice has accreted, but computational based prediction models such as LEWICE are available [15]. In all three ice regime cases there will be a defined main body of ice along with the formation of ice feathers. These feathers are delicate, single columns of ice crystals that build up behind the main body of ice.

Rime ice formation is normally encountered when the ambient temperature is low, the LWC of the cloud is low, and the MVD of the water particles is small. These conditions result in a freezing fraction that is said to be unity (equal to 1). In this icing regime, water particles freeze to the rotor surface upon impact and tightly conform to the shape of the leading edge. Due to the water particles freezing upon impact, air becomes trapped in the formation and gives an opaque milky appearance to the ice. The surface of the formation is normally rough leading to an increase in drag experienced by the airfoil [15]. A typical rime ice formation is shown in Figure 1.2c.

Glaze ice formation is normally encountered when the ambient temperature is close to the freezing point of water, the LWC of the cloud is high, and the MVD of the water particles is high. These conditions result in a freezing fraction that is said to be less than unity (less than 1). In this icing regime, water droplets are no longer capable of freezing upon impact. Instead, they splash after impacting the

surface and run back along the blade as a thin liquid film until eventually freezing. This results in large horns forming. Since the ice is taking a longer time to freeze, air is no longer being trapped and the ice appears clear in color. Because of the horn shape, glaze ice typically causes the largest aerodynamic penalties of the 3 regimes [15]. A typical glaze ice formation is shown in Figure 1.2a.
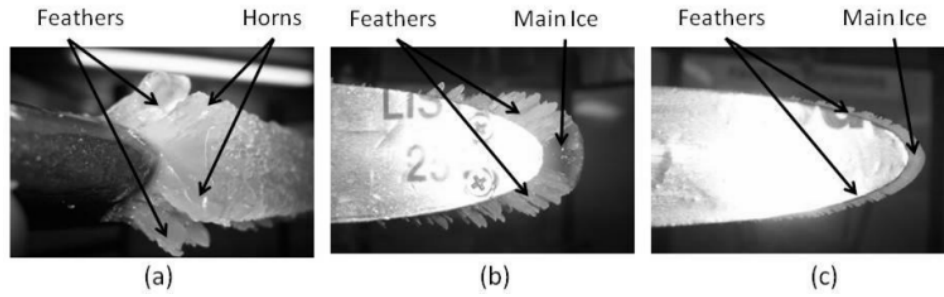
Figure 1.2. Ice Regimes: Glaze (a), Mixed (b), Rime (c) [2]

There is no distinct transition point defined by a combination of conditions that yield a mixed ice regime. Instead mixed ice is defined as a transitions region between glaze and rime. Normally mixed ice will have a main ice shape that is clear in color like glaze ice and feathers behind the main shape that are similar to those formed in rime ice. A typical mixed ice formation is shown in Figure 1.2b.

The relationship between the three icing regimes and the icing conditions which create them can be seen in Figure 1.3. It is important to note that this figure is only a loose guideline.
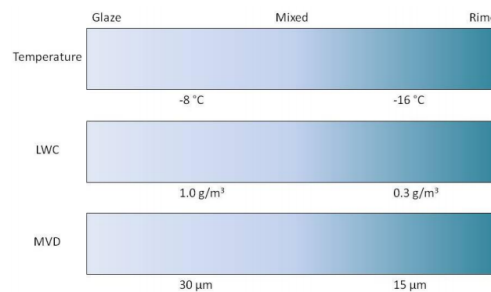
Figure 1.3. Ice Regime and Condition Relationship [2]

1.2.3 Material Properties of Ice

To properly model ice accretion over the leading edge of an airfoil, shed ice length, trajectory, and impact, the material properties of ice must be known. Many papers have been published on ice properties over the last few decades. Yet, the results of similar tests reported in these papers are either contradictory or vary greatly. In general, this is due to different methodologies being used in the studies for testing the same property.

Ice is a complex material by nature. This is due to the material properties being a function of the test conditions in which the ice was created. Differences in temperature, grain size, porosity and crystalline orientation all affect the value of the material property being measured. To further complicate the problem, the stress-strain relationships of ice are rate-sensitive, which means they are also a function of the rate of deformation. This makes determining the elastic behavior from the rate dependent effects difficult [16].

In spite of this complex nature, enough knowledge has been developed to permit predictions of ice behavior. There are two basic categories of icing models, physical and empirical. Physical models are the more complex of the two. They require specific knowledge of the test conditions, parameters such as: ambient temperature, LWC of the cloud, MVD of the water particles, and velocity. These types of models normally require significant computational power and have become more accurate as computing power has increased. The second type of models are based on empirical and statistical trends. Given the amount of computational power available today, physical models are more widely used [16]. The subsections that follow will discuss three key material properties of ice and the variables which influence their value.

1.2.3.1   Elastic Modulus of Ice

There are two common methods for determining the elastic, or Young's, modulus of a material. A static method which involves using Hooke's law of elasticity, and a dynamic method which involves measuring the velocity of two propagating waves. Using Hooke's Law is not only simpler but generally gives a more accurate value. Determining the elastic behavior of a homogeneous and isotropic material requires specific knowledge of two independent elastic constants. The elastic modulus is one and typically Poisson's ratio is the other. Elastic constants are defined for isotropic materials only and ice is only truly isotropic when the orientation of the crystals in the structure of the ice is completely random [16].

The elastic modulus of fresh water ice has been measured to be anywhere from 2 GPa for loading at low frequencies, all the way to 9 GPa at high frequency. Poisson's ratio ranges from 0.29-0.32. A final important note regarding the elastic modulus is that rate of loading, temperature, grain size and type will all effect the measured value [16].

1.2.3.2   Tensile and Compressive Strength of Ice

Ice normally behaves as a brittle material, but under very special circumstances can also behave as a ductile material. As a brittle material, compressive and tensile ice strengths seem to be dependent on grain size, strain rate, volume and temperature [16]. Different researchers report immensely different values of ultimate tensile strengths of impact ice as seen in table 1.1.

Table 1.1. Comparison of Ultimate Tensile Strengths of Impact Ice by Different Researchers.

Researcher	Average Ultimate Tensile Strength of Impact Ice (MPa)
Reich [17]	1.37*/0.13**
Chu et al. [18]	0.22*/0.20**
Druez et al. [19]	1.62*/2.66**
	(* - glaze, ** - rime)

In addition to the large variation in reported values, the sample size of the values reported compared to that of other properties, such as elastic modulus, is very small.

1.2.3.3 Adhesion Strength

Like the tensile and compressive strengths of ice, adhesion strength of ice is dependent on a variety of test conditions. There is also a significant variation in the reported adhesion strengths by different researchers. Brouwers et al. [20] summarized this inconsistency for ice adhered to an aluminum plate at -11°C in Table 1.2. There are many factors that can be affecting the variation in results. For instance, some of the methods involve accreting ice in one facility, and then transporting it to some type of removal rig. During the transportation mechanical and thermal stresses can be introduce to the ice, creating sources of uncertainty. The ice removal method must be taken into account. A system which uses a mechanical force may apply moments which are not accounted for and result in extremely low strength measurements. Another factor which must be accounted for is surface roughness. In many of the tests performed, researchers have not taken into account surface roughness of the material on which they were accreting ice.

Table 1.2. Literature Values for Shear Adhesion Strength of Ice on Al. (T=-11°C)

Researcher Date [Reference]	Test Type	Type of Ice	Shear Adhesion Strength psi (kPa)
LoughBorough 1946 [21]	Pull	Freezer Ice	81 (558)
Stallabrass and Price 1962 [22]	Rotating Instrumented Beam	Impact Ice	14 (97)
Itagaki 1983 [23]	Rotating Rotor	Impact Ice	4-23 (27-157)
Scavuzzo and Chu 1987 [24]	Shear Window	Impact Ice	13-42 (90-290)
Reich 1994 [25]	Pull	Freezer Ice	130 (896)

In an attempt to remove many of the sources of uncertainty associated with previous research on ice adhesion strength, Soltis et al. [3] developed methodology for a novel hands-off approach. By removing interaction between the accreted ice and the outside influence of moving ice from one facility to another, there will be no unintentional introduction of mechanical and thermal stresses. The methodology uses the AERTS facility to mimic in flight ice accretion on rotor blades. The ice is then shed naturally due to centrifugal forces. The exact details for measuring the adhesion strength after the ice has shed can be found in source [3]. By using the centrifugal force to shed the ice, unintended forces and moments seen in mechanical test types are not introduced. In addition, AERTS features precise control of the test conditions including: temperature, LWC, MVD, and rotor speed. This along with the methodology developed by Soltis et al. has led to AERTS becoming one of the premiere test facilities for ice adhesion strength testing of coatings and materials. Using this new methodology and state of the art facility, Soltis et al. documented the effects of LWC, MVD, temperature, surface roughness, and grain orientation on adhesion strength with a much greater amount of consistency then

in previous research.

As the density of super-cooled water droplets in a cloud increases, so does the rate at which they impact surfaces. This results in a greater amount of heat transfer from the droplets to the impact surface and subsequently a decrease in the adhesion strength of ice. This is most evident for extreme LWC values ($>5\text{g/m}^3$). Since extreme values of LWC are not encountered in a natural icing environment, the effects of LWC variation seen by helicopters in the range of the icing envelop is of greater interest. Shown in Figure 1.4, variation of LWC in this range has no effect on ice adhesion strength [3].
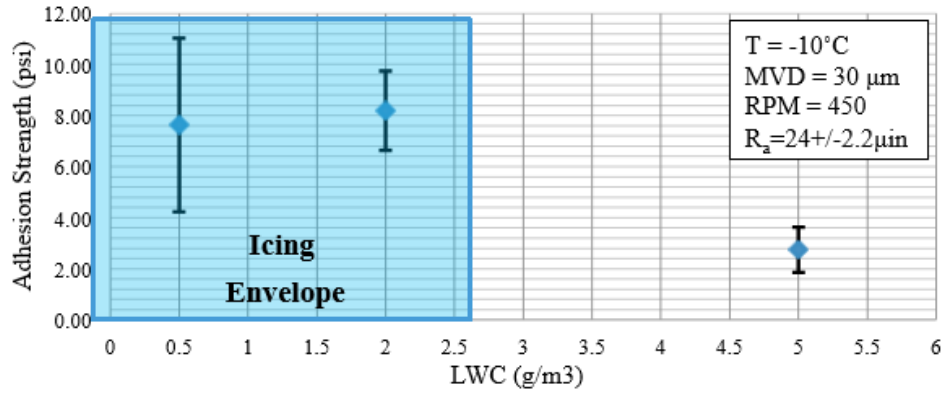
Figure 1.4. Effects of LWC on Ice Adhesion Strength [3]

Varying temperature and MVD results in a negative linear correlation with ice adhesion strength, while increasing surface roughness and grain orientation results in a positive linear correlation. The experiments performed by Soltis et al. showed that adhesion strength decreased by 65% as MVD increased over a range of 20 to 40 μm (Figure 1.5), increased 670% when temperature was decreased from -8°C to -16°C (Figure 1.6), and increased 250% as surface roughness was increased from 24 to 105 μin (Figure 1.7). It was also seen that as grain orientation increased from 0° to 90° ice adhesion strength increased [3].
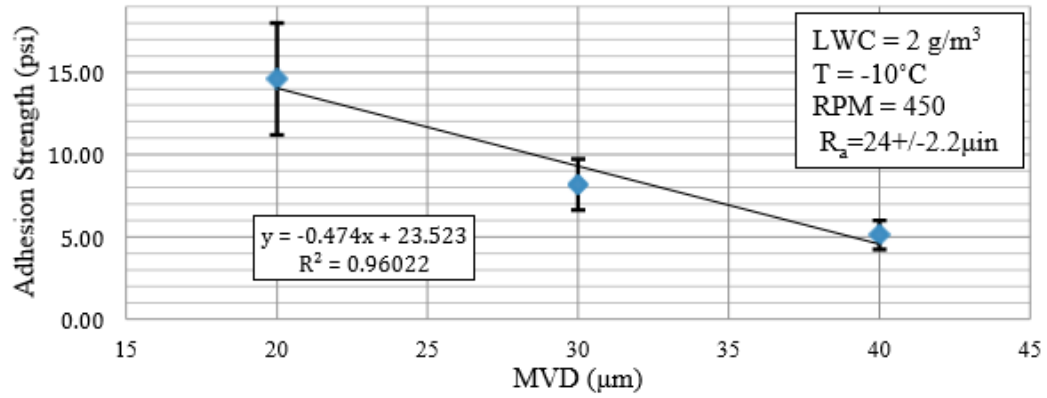
Figure 1.5. Effects of MVD on Ice Adhesion Strength [3]
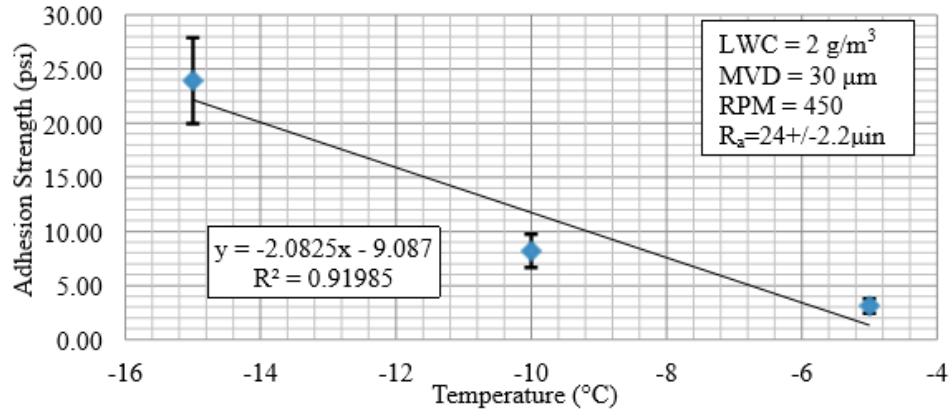
Figure 1.6. Effects of Temperature on Ice Adhesion Strength [3]
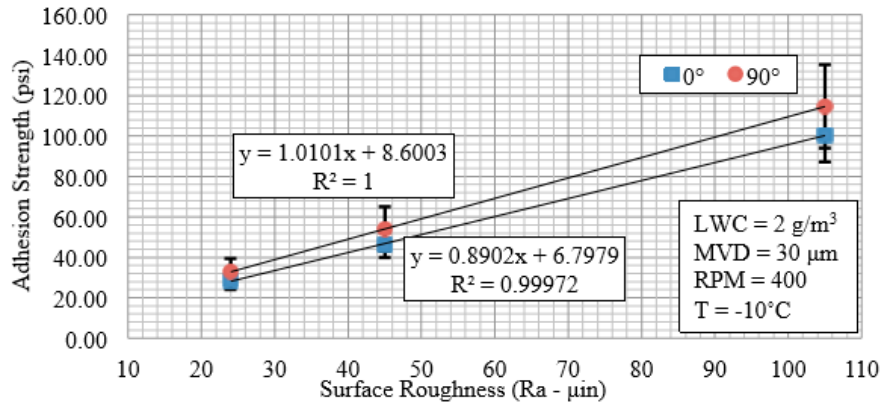
Figure 1.7. Effects of Surface Roughness and Grain Orientation on Ice Adhesion Strength [3]

1.2.4 Performance Degradation Due to Icing

The airfoils used on rotorcraft are designed, tested, and optimized for performance in a clean condition. As ice accretes on the blades, the shape of the airfoil is changed and what was once a high performance airfoil has now been significantly degraded. Significant accretion will result in controls becoming sluggish which makes piloting the rotorcraft difficult and even dangerous. In addition, a rotorcraft with blades that have not been equipped with a de-icing system will be subject to natural ice shedding. Natural ice shedding occurs when the amount of accreted ice reaches a critical value. This critical value is when the adhesion strength of the ice to the blade is exceeded, typically by centrifugal force. While this may seem beneficial, natural shedding does not normally occur symmetrically. Non-symmetric shedding will result in severe vibration that will not only be uncomfortable for the pilot and passengers but also creates rotor imbalance [26].

Han et al. recently performed wind tunnel experiments which show the variations in performance due to ice accretion. In these experiments, ice was accreted onto a NACA 0012 airfoil using the Pennsylvania State University Adverse Environment Rotor Test Stand. This ice was then cast in a hard plastic and placed in a wind tunnel for testing [4]. One of the ice shapes that was accreted and tested can be seen in Figure 1.8. In addition to the ice shape the figure also displays computer predictions of what the shape should look like given the testing conditions.
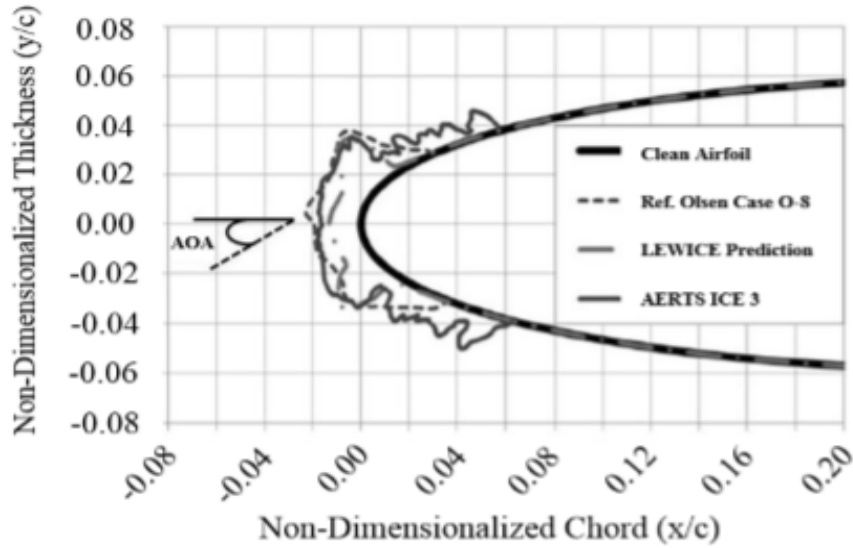
Figure 1.8. Example Ice shape Tested by Han et al. [4]

The aerodynamic performance was documented over a range of angles of attack. The effects on drag, lift, and pitching moment can be seen in Figure 1.9. Due to the ice shape on the leading edge of the airfoil, there was a slight increase in drag below angles of attack (AoA) of 6°. As the angle of attack increased past 6°, the drag coefficient (C_d) significantly increases. Before stall of the airfoil, 15° AoA, a wake survey to measure drag was performed. The results showed that for this icing case the drag was nine times higher than the clean airfoil. The lift coefficient (C_l) is seen to be slightly lower than the clean airfoil below a 6° AoA. As the AoA was increased, the lift coefficient significantly decreased and just before stall the C_l was measured to be 35% lower than the clean airfoil. The pitching moment (C_m) of the clean airfoil stayed relatively constant until stall. With the introduction of an ice shape, the pitching moment varied widely based on the AoA.

These results are important because the power required for flight will change. Increased drag and decreased lift result in a significant increase in power required to maintain flight. If this power requirement is greater than the available power, the

aircraft will be forced to descend and could result in a crash. A pitching moment which varies based on AoA will constantly change the required lift which in turn will change the power requirements.
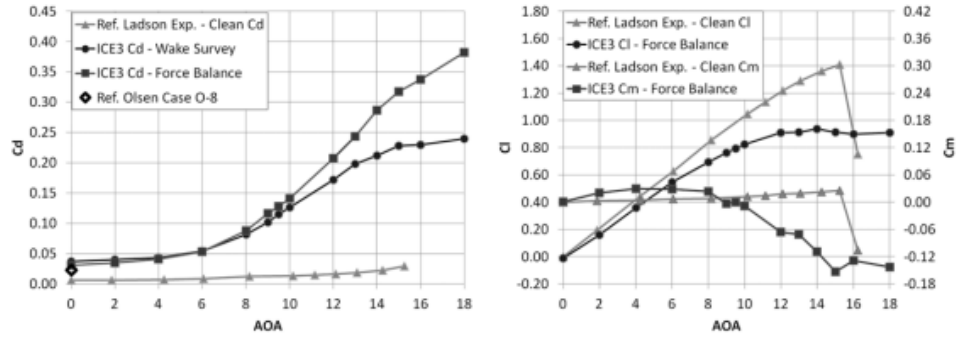
Figure 1.9. Left: Drag Coefficient vs. AOA. Right: Lift and Pitching Moment Coefficients vs. AOA. [4]

1.3 Rotorcraft Ice Protection Systems

To address the adverse effects associated with icing and to minimize their impact, it is important for aircraft and rotorcraft to have some type of ice protection system (IPS). IPS's are split into two categories. The first category consists of anti-icing systems. These are ideal because they prevent any ice from accreting and therefore no impact to the aerodynamic performance. The major drawback with these types of systems is they are highly susceptible to erosion. Examples of anti-icing systems include low ice adhesion coatings and fluid de-icing systems. The second, more common type of IPS's are de-icers. These systems allow ice to build up and then induce shedding in a symmetric fashion. The major drawback is that these systems require power. The most common form of de-icing system for a rotorcraft is electro-thermal. Other examples include pneumatic, electrovibratory, electro-impulsive, and ultrasonic.

1.3.1 Low Ice Adhesion Coatings

Low ice adhesion coatings (also called ice-phobic coatings) have a wide variety of application and are the only true passive form of an IPS. The general idea behind this type of protection system is to lower the adhesion strength of ice to the surface. The lower the adhesion strength is, the faster natural shedding will occur. Consequently, there will be less ice build up and a smaller impact to aerodynamic performance. This also helps to mitigate the effects of non-symmetric shedding. Low ice adhesion coatings are extremely susceptible to erosion. Rotorcraft blade erosion protection is very import and cannot be compromised for a leading edge low adhesion coating. For this reason, coatings must be tested before and after erosion to determine effectiveness.

Research on these types of coatings dates back to the 1920's. One of the first tests in the icing research tunnel investigated six insoluble and five soluble compounds for preventing ice accretion. The insoluble compounds that the researchers tried were light and heavy lubricating oil, grease, vaseline, paraffin, and simonize wax and the five soluble compounds were glycerin, glycerin mixed with calcium chloride, molasses mixed with calcium chloride, a hardened sugar solution, and a hardened glucose solution. All of these compounds proved disappointing as none of them prevented ice accretion. Other various compounds tested were honey, corn syrup, glycerin soap, commercial paint, and goose grease [8].

More recently, a wide range of materials that have potential as low ice adhesion coatings for rotorcraft blade leading edges were tested by Aviation Applied Technology Directorate (AATD), Boeing, and The Pennsylvania State University. The test results showed that the materials worked well after initial application. Unfortunately significant erosion occurred after repeated testing and the resulting

adhesion strengths were significantly higher. The results of the tests can be seen in Figure 1.10 [2].
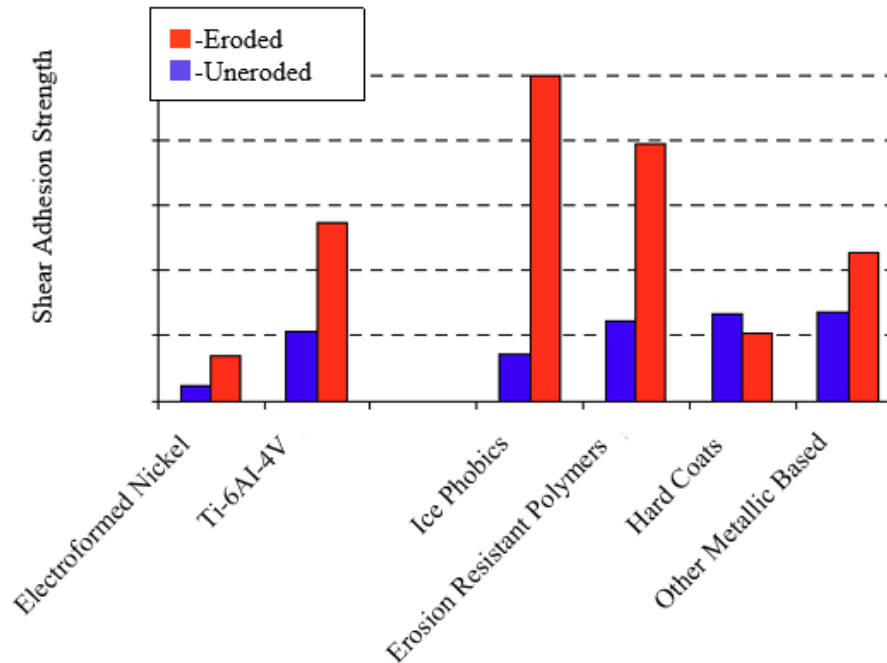
Figure 1.10. Adhesion Strength Degradation for Potential Leading Edge Materials [2]

1.3.2 Fluid De-Icing Systems

In the early 1960s, Bell Helicopter began developing a fluid de-icing system for use on the main and tail rotors of the HU-1, later renamed UH-1. The idea was to prevent ice accretion by continually pumping fluid through a porous leading edge and letting the fluid flow down the blades span. The system consisted of an 11 gallon reservoir containing a mixture of alcohol and glycerin. The mixture was pumped from the reservoir to the main and tail rotors using an electric pump that was rated for 43 gal/hr at 15 psi. The flow rate of the fluid was monitored using pressure gages and controlled using flow valves. To move the fluid from the fixed frame of the rotorcraft to the rotating frame of the rotors, a pneumatic

slinger ring was used. A schematic for the system can be seen in Figure 1.11. The rotor blades were modified to allow the fluid to be distributed along the blade and was accomplished by milling grooves into the front and back surfaces of the blade nose block and by drilling holes into the leading edge. This allowed the anti-icing mixture to flow through the grooves in the nose block, escape through the holes in the leading edge, and flow over the surface of the blade. This system was successfully tested at the Ottawa spray rig for temperatures down to -20°C and LWC's up to 0.8 g/m^3 [5].
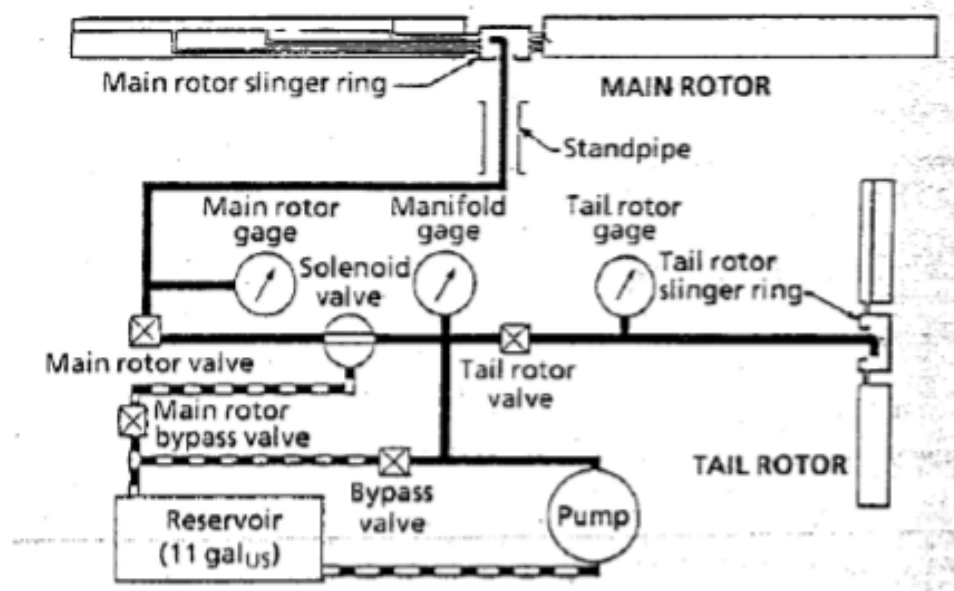
Figure 1.11. Schematic of Fluid Anti-Icing System [5]

Fluid de-icing systems provide continuous prevention of ice accretion. This makes them one of the only practical anti-icing systems available for rotorcraft. In addition to preventing the build up of ice, these systems can also be used as blade de-icer up to an ice thickness of 0.3 inches. This flexibility results in minimal degradation of the aerodynamic properties of the rotor blades. Other advantages include low power requirements and the absence of water run back, which can

freeze on unprotected areas of the blade. Unfortunately, there are several key disadvantages which prevents this type of system from being feasible for most practical applications. The biggest disadvantage of the system is the nature of fluid itself. The fluid needs to be stored on the rotorcraft which results in a weight issue. Since only so much fluid can be carried at a time, the amount of ice protection time is consequently limited. In the case of the previously described system, the 11 gallon tanks could only hold enough fluid for 84 minutes of ice protection. Other disadvantages include the need for pneumatic slip rings and the tendency of the leading edge holes to become clogged with dirt particles [5].

1.3.3 Pneumatic Boots

Pneumatic deicing systems have primarily been used on fixed wing aircraft. These systems are attractive options due to being light-weight, low cost, and requiring a low amount of power to operate. Pneumatics are less attractive options for rotorcraft due to how easily they erode. Goodrich developed pneumatic boots that were similar to those used on fixed wings for use on a UH-1H helicopter. These pneumatic boots were placed chordwise along the span of the leading edge and can be seen in Figure 1.12. The system works using bleed air from the turbine engine to inflate the boots. Boot inflation takes approximately 2 seconds and the time between inflation and deflation is 30 seconds. The boots were successfully tested at the Ottawa spray rig and the U.S. HISS. Ice was accumulated to a thickness of 0.3 inches at an LWC of 0.8 g/m^3 and a temperature of -20°C and successfully shed [5].
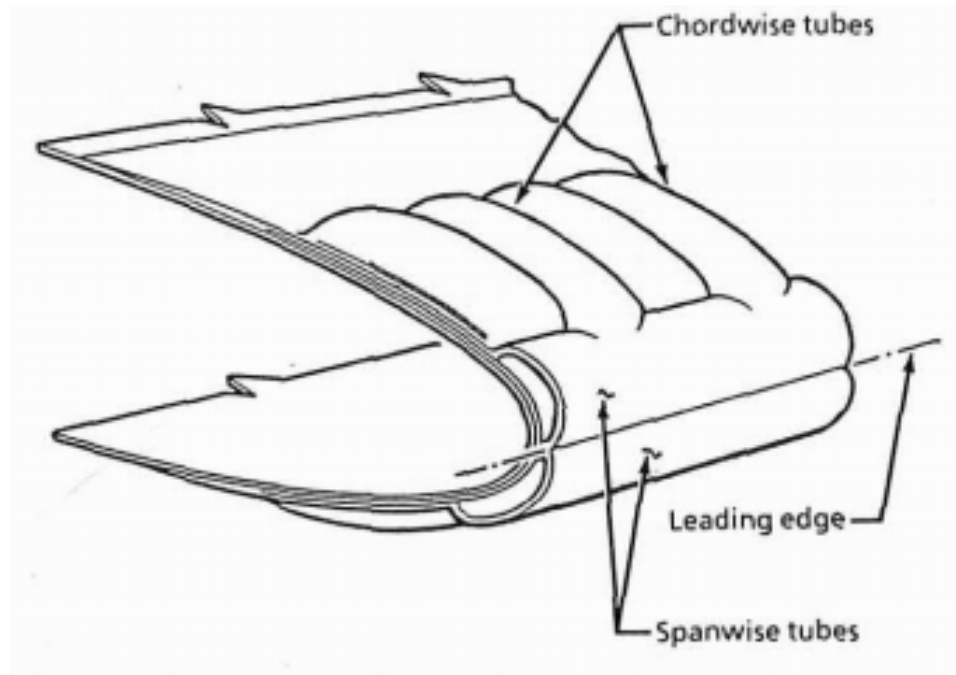
Figure 1.12. Pneumatic Boot de-icing System for UH-1 [5]

1.3.4 Electro-Impulsive

Electro-impulse ice protection systems use electro-magnetic fields to de-ice the leading edge of aircraft wings. This is accomplished by placing flat-wound coils made from copper ribbon wire inside the leading edge of a wing, as seen in Figure 1.13. They are typically attached to a front spar, a beam attached to ribs, or directly to the skin itself and there is typically a 1 mm gap between the coils and the skin. Depending on the size and shape of the leading edge either one or two coils are placed at a given "span-station". The coils connect to a bank of high voltage capacitors. When these capacitors are discharged through the coils a magnetic field rapidly grows and decays. This induces eddy currents in the metallic skin which opposes the magnetic field in the coils creating a repulsive force of a few hundred pounds. This repulsive force only lasts a fraction of a millisecond and causes the skin to quickly accelerate outward a small amount. This will delaminate the ice

and shed it from the airfoil. Two or three of these impulses are normally required and then ice is allowed to re-accumulate until a critical size is again reached [5].
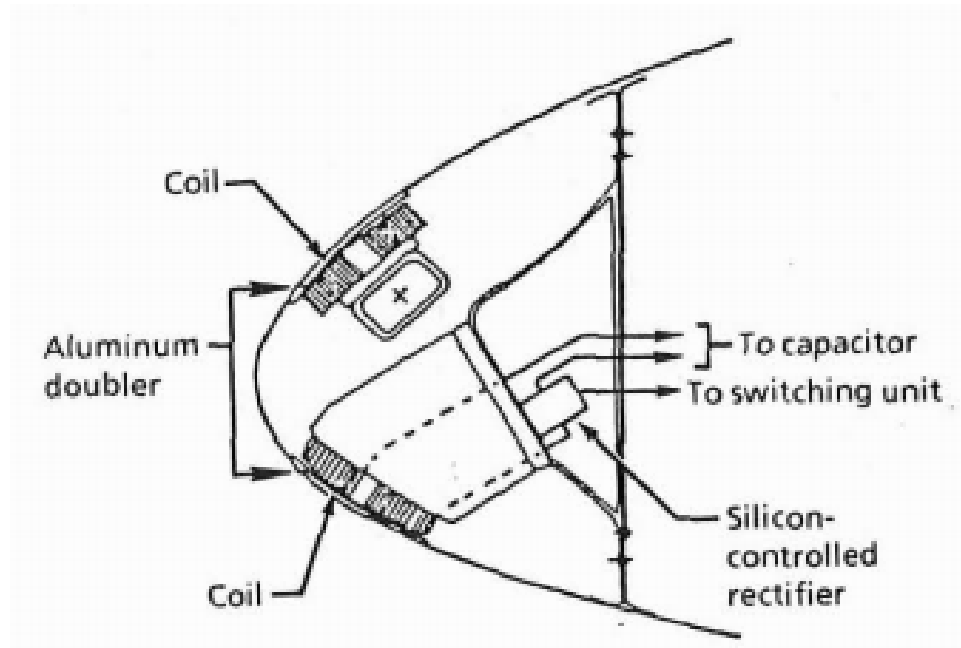
Figure 1.13. Schematic of Impulse Coil Installation [5]

Electro-impulse ice protection systems need approximately 1 kW of power for general airplane and 3 kW for medium sized helicopters. While the low power requirement makes these types of systems very attractive, they are rarely used on rotorcraft. The task of installing one of these systems in a rotor blade is much more difficult than for a normal aircraft. Rotor blades are significantly smaller then aircraft wings so there is already less room to work. In addition the leading edge is solid to support banding loads as opposed to that of a fixed-wing aircraft which can be hollow. Removing material from the leading edge to make room for coils and drilling holes to run the wires decreases the stiffness of the blade. This can lead to a fatigue failure due to stress [5].

1.3.5 Electrovibratory

Electrovibratory de-icing systems were first studied in 1978 by Bell Helicopter for use on the main rotor blades of the UH-1H. In this study, Bell used a mechanical shaker mounted at the root of the blade and matched the frequency of the shaker to the major natural frequencies of the blades in order to maximize blade deflection. For the study four different shaker locations were considered, as seen in Figure 1.14. The shaker was driven by a 0.5 hp motor and consisted of two 1.25 lb eccentric weights. Bell estimated that a flight-worthy system for the Uh-1H would weigh 67 lbs and need about 1.3 kW of power. The shaker was activated for 2s at forces up to 35 $g's$ and was tested between -5°C and -15°C. Results showed that the blade was adequately deiced everywhere except for the tip. The main concern with this type of system is rotor blade fatigue [5].
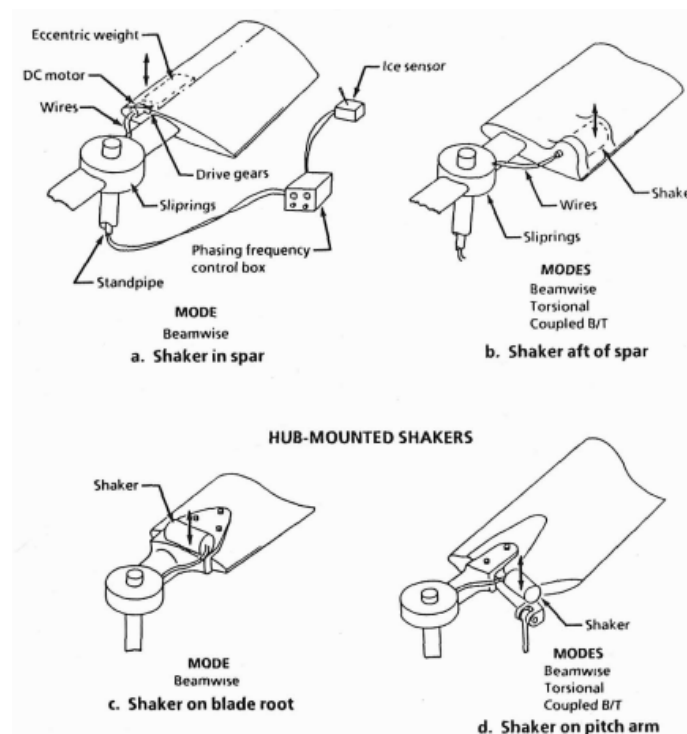
Figure 1.14. Shaker Mounting Locations [5]

1.3.6 Piezoelectric Ultrasonic

Piezoelectric materials (PZT) build an electric charge when strained. This effect is used in many sensors and energy harvesters. When the effect is reversed and an electric potential is applied to the PZT, it will strain. An ultrasonic de-icing system works by actuating PZT's that are bonded to the skin of the leading edge, as seen in Figure 1.15. This creates vibration and induces a transverse shear stress that sheds the ice. Recently, work performed by Palacios [27], Overmeyer [6], and Soltis [2] at the Pennsylvania State University has led to the development of an ultrasonic de-icing system which uses lead zirconium titanate (PZT-4). PZT-4 was chosen due to having a large stiffness and for its block force capability. The system was tested using the AERTS facility and demonstrated the ability to de-ice rotor blades over a wide range of icing conditions. The system performed effectively using a max input power of 6.65 W/in^2 [27].
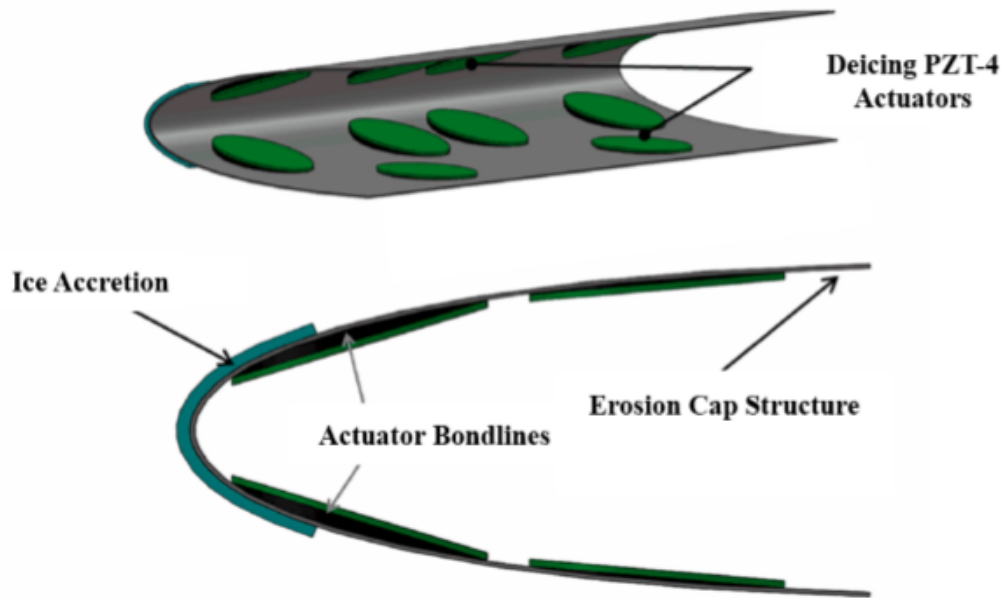
Figure 1.15. Schematic of Ultrasonic De-Icing Actuators on Leading Edge [6]

1.3.7 Electro-thermal

The most common type of IPS is an electro-thermal de-icing system and it is the only system certified for use on commercial and military helicopters [5]. An electro-thermal de-icing system works by sending an electrical current through resistive circuits known as heating elements. The resistors in these heating elements convert electrical energy into thermal energy. This process is called resistive heating and is also known as the Joule heating effect. The heating elements are normally bonded to the inside surface of the leading edge skin to protect them from erosion. The heat created by the elements is transferred through the skin and to the ice surface by conduction. A simple schematic of this type of system can be seen in Figure 1.16. Early electro-thermal IPS's consist of foil and wires laid in grid patterns for even heat distribution. Most heating elements today are made of carbon fiber composites and these may eventually be replaced by carbon nano tubes (CNT) [28].

Figure 1.16. Simple Schematic of Electrothermal IPS [2]

In an ideal world, electro-thermal IPS's would be used as an anti-icing system by applying continuous heat over the entire blade and preventing any ice from forming. The electro-thermal systems currently in use, such as the one used on the UH-60, have enormous power requirements (25 W/in^2) [29]. Since this is impractical, the heaters are broken up into either span-wise or chord-wise elements and ice is then

allowed to accrete to approximately 0.3". The heaters are then cycled and the ice is shed. The challenge with cycling the heaters is determining when and how long to apply heat in order to avoid water run-back which results in significant loss of aerodynamic performance. While this method saves a significant amount of power, a normal helicopter will still require large auxiliary power units which increase the weight of the aircraft [5].

Development of one of the first conventional electro-thermal systems was contracted out to Sikorsky in the late 1970s by the U.S. Army for use on the UH-60 Black Hawk. The contract required that the helicopter function in icing conditions as cold as -20°C and for clouds with LWC up to 1.0 g/m^3. Sikorsky responded with a main and tail rotor protection system using electro-thermal de-icers as well as an engine inlet protection system. The initial design protected only the outboard section of the blades which allowed all four blades to be de-iced at the same time. In 1976 the systems were flight tested for four hours in icing conditions in Alaska. This resulted in the engine inlet IPS being certified for use. During the tests however, it was documented that the inboard section of the rotor blades saw a significant increase in torque due to the accreted ice and that additional span-wise protection would be required. After extending coverage to the entire length of the blades, they could only be heated in pairs due to the significant increase in power required. The rotor protection system was certified for use in 1981 [29].

In the early 2000's a non-conventional electro-thermal system known as the Low Power Electro-thermal De-icing (LPED) system was developed by Goodrich. This system does not send a continuous AC or DC electric current to the heating elements over a specified time and cycling pattern like a conventional system would. Instead the LPED system uses a pulsing technique where both anti-ice and de-ice heaters are utilized. The anti-ice heaters are located along the stagnation region

of the airfoil and are known as parting strips. These heaters are pulsed for a few milliseconds and they essentially split the ice buildup into an upper and lower cap. The de-icing heaters are placed adjacent to the leading edge region in segments and are used to shed the ice caps. This is done by sending them short pulses of high amounts of power, melting the interface of the ice on the leading edge. The force due to drag then removes the ice. Another difference between the LPED system and a more conventional one is that LPED heating elements are applied directly to the outside of the leading edge skin. This minimizes the thermal energy lost through conduction and increases the overall performance of the system. The LPED was flight tested during the winter of 2003 and 2004 using a fixed wing aircraft. The system was powered using a bank of 3500 farad capacitors which were discharged in 1.4 seconds every 3 minutes. This allowed the LPED to shed ice just as effectively as a conventional system, but using 20-50% less power [30].

The next generation electro-thermal de-icing system being developed involves using carbon nanotubes (CNT) to make up the heater elements. In order to create these new heater elements, CNTs are first grown to heights of 80 to 100 μm on silicon wafers. Next, a sheet of nonporous Teflon is placed over the CNTs. Finally, a small radius steel tool is used to compress the CNTs onto the silicon wafer to create a heater element patch. Larger heater elements were built by placing these patches next to one another on an epoxy film and cured. In 2013, the larger heater elements were tested in the Cox icing wind tunnel. Two elements were bonded to the surface of a wing section and subjected to temperatures ranging from -3 to -20.5°C. The heaters were shown capable of anti-icing as well as de-icing. Unfortunately the tests also showed ice bridging to unprotected areas of the wing section as well as islands of ice building up [28].

1.4 The Ice Impact Problem

Shedding of accumulated ice becomes a ballistics concern, especially in helicopters. In the case of conventional helicopters, rotor blade tip speeds can reach speeds in excess of 200 m/s (447 mph). Large enough ice particles flying off the blades at this speed can seriously damage the tail rotor and tail assembly (also known as the empennage) in conventional helicopters, and the fuselage in tiltrotor configurations. The ice impact problem has three stages: the delamination and shedding of ice from the blade, break up and trajectory of the shed ice, and finally impact.

1.4.1 Delamination and Shed

Delamination of ice affects the aerodynamic performance of the rotor blades, causes loads on the blades to change, and introduces vibration. This has led to a significant amount of research in developing prediction tools for both delamination and shedding. Finite element analysis (FEA) has recently been used to create prediction models for propagation of cracks and delamination growth.

Shiping et al. developed a three dimensional FEA code based on fracture mechanics to predict ice crack growth. They used an in house icing prediction code called FENSAP-ICE to simulate ice accretion. The code is a computational fluid dynamics (CFD) package that solves the Navier-Stokes equations, determines the water droplet trajectories, and predicts the formation of ice. The ice shape was then meshed with linear tetrahedral elements using a Galerkin approach. The simulation was then run adjusting the stress in the ice based upon the crack and delamination growth until the ice ultimately failed [31].

Empirical models derived from experiments and statistics have also been developed. The Pennsylvania State University was able to match shed time and location to in-house experiments performed on the Adverse Environment Rotor Test Stand within 25% using their Rotor Icing, Shedding and Performance (ARISP) model. A correction factor ended up being added due to the model over predicting the amount of ice accreted at the tip of the blade [20]. Bain et. al. predicted the performance of a flexible rotor under icing conditions in forward flight by developing a computer program. The program uses LEWICE3D to predict the ice formation and two CFD solves, OVERFLOW and GT-Hybrid. The CFD solvers were loosely coupled with a computational structural dynamics solver called DYMORE. This was necessary to include the structural dynamic effects of the rotor. The rotor was modeled using six degrees of freedom and was subjected to icing. The stress field was analyzed at each time step until shedding occurred. The model under predicted shedding time and over predicted both shed ice length and ice thickness along the span of the blade [32].

1.4.2 Break-Up and Trajectory

After ice delaminates from the blade surface, centrifugal force causes it to slide down the blade and past the tip. Once past the tip, it is exposed to drag and breaks into smaller pieces. This was first observed at the NASA Glenn Icing Research Tunnel while testing a Bell 206B tail rotor [7]. Shown in Figure 1.17, the shed ice breaks up into smaller pieces as it moves past the tip of the blade. These small pieces of ice can still cause damage to the rotorcraft. Developing a way of predicting the size of ice as its shed and leaves the tip of the blade is the focus of this thesis.
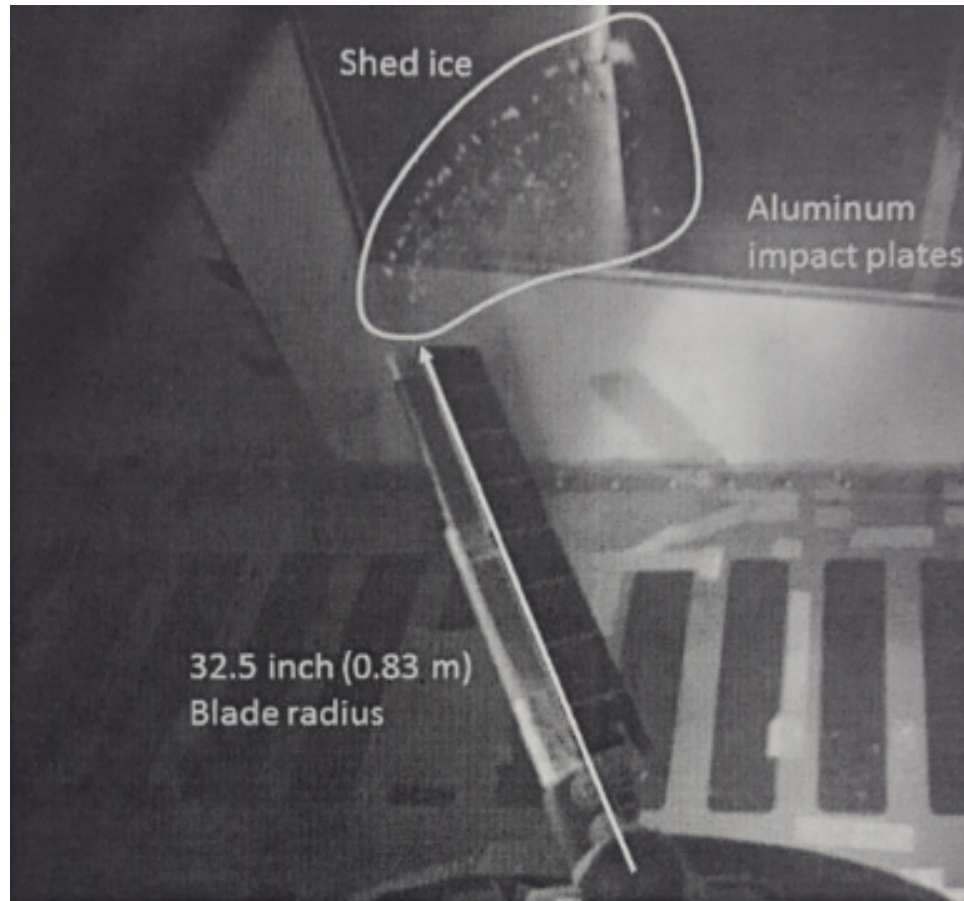
Figure 1.17. Ice Breakup during Bell 206B Tail Rotor Icing Test [7]

Being able to predict the trajectory of the pieces of shed ice is important to determine if the rotorcraft will get damaged. Baruzzi et al. developed a numerical approach to simulating shed ice trajectories using an in-flight icing code known as FENSAP-ICE. In this approach, FENSAP-ICE is used to mesh the moving domains into a fixed background mesh. This is done by using a hole-cutting and stitching algorithm to create a continuous unstructured hybrid mesh which has no interpolation points [33].

1.4.3 Impact

Ice particles that are shed from a rotor blade will have a high velocities and therefore, a large amount of kinetic energy. Particles that impact the surfaces of the vehicle have the potential to cause damage. In the event of impact, manufacturers need to know how much damage the ice is capable of producing. This has resulted in an extensive amount of research.

Researchers at NASA Glenn used the IRT to conduct impact tests on an OH-58 tail rotor. Their goal was to create a database of impact force and energy for both natural and forced shedding of ice. Forced shedding of ice was accomplished using a pneumatic boot de-icing system manufactured by Goodrich. Force sensors were mounted to the test section side walls to capture the force time history of impact and high speed cameras were used to measure the ice particle size and its velocity. The researchers measured peak forces that ranged from 2.2 to 890 N [34].

Researchers at the University of Toledo developed an alternate approach to modeling ice impact by using a pneumatic ice gun. Pressurized air is used to accelerate the particles down the gun barrel. The exit velocity is determined using a velocity sensor at the tip of the barrel, and is controlled by increasing or decreasing the pressure in the tank. Pellets of varying mass of glaze type ice were used and were impacted on tempered sheets of aluminum to simulate ice striking an airframe. Force sensors similar to the ones used for the OH-58 tail rotor test were mounted to these aluminum plates to capture the force time history of the impact. The test results using the ice gun were compared to those from the OH-58 tail rotor tests. In addition, a finite element code called DYNA3D was used to predict ice impact loading and damage [35].

1.5 Thesis Objectives

Current ice accretion tools can predict the cross-sectional shape of ice accreted on a blade however, the size of shed ice after leaving the tip of the blade remains unknown. The main goal of this thesis is to develop a tool to predict the projectile size of ice fragments that have broken off the tip of a rotating blade after the main ice body has been shed. Given the large variation and small sample size of the ultimate strengths of impact ice that is reported in literature, a secondary goal will be to determine this value experimentally.

To achieve these goals, the following objectives must be met:

1. Determine whether the ice projectile is created due to transverse shear or tensile stress on the sliding ice column and develop a mathematical model to predict such critical length.

2. Experimentally determine the ultimate strength of impact ice.

3. Experimentally measure the length of broken ice as it leaves the rotor blade using high-speed cameras.

4. Acquire the cross-sectional properties of the ice shed.

5. Compare experimentally measured lengths to model predictions during model validation efforts.

1.6 Thesis Overview

1.6.1 Chapter 2: Ice Fracture Modeling

Two mathematical models were explored while developing a prediction tool for determining the size of shed ice from a spinning rotor blade. A model based on an Euler-Bernoulli tensile strength failure was compared to a model based on Timoshenko transverse shear failure.

1.6.2 Chapter 3: Experimental Testing

In chapter 3, an overview of the testing facility and testing procedure is presented. The test matrices for the experiment are laid out and the methodology used to take measurements is described.

1.6.3 Chapter 4: Results and Model Validation

In chapter 4, experimental results and the predictions from the model are compared and discussed.

1.6.4 Chapter 5: Conclusions and Recommendations

The final chapter discusses conclusions drawn from this research and offers recommendations for future work to increase the effectiveness of the prediction model.

Chapter 2 |
Ice Fracture Modeling

2.1 Model Development

The goal of this chapter is to present a model for predicting the length of fractured ice that is shed from the tip of a rotating blade. The model is based on the stresses created by aerodynamic forces on the overhanging ice shapes exceeding the strength of the ice.

2.1.1 Problem Overview and Considerations

A rotor blade subject to icing conditions will accrete ice along the leading edge of the blade. At some point this ice will have to either shed naturally, or be induced to shed using icing protection systems. When the ice sheds, it slides off the blade and breaks into smaller pieces as it travels over the tip. These small pieces have now become projectiles. Knowing the length of these projectiles is key to determining their trajectory and the impact damage they could cause.

A rotor blade with a symmetric airfoil cross-section that is spinning at zero angle of attack, has negligible lift force. Therefore, the only significant forces

acting on the blade are drag (along the leading edge) and centrifugal force (pulling outward from the center of rotation), shown in Figure 2.1. The drag force increases along the length of the blade due to the linear increase of velocity as the span-wise location from the rotor increases. The centrifugal force will also increase, but will be due to the increase in mass as you move radially away from the hub.
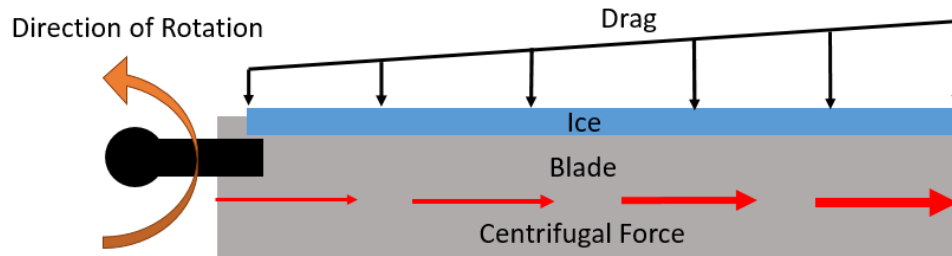
Figure 2.1. Top View Diagram of Blade with Ice Before Shedding

When the ice is shed, both of these forces are still acting on the ice. As seen in Figure 2.2, the centrifugal force causes the ice to slide down the leading edge towards the tip and the drag force prevents it from becoming dislodged from the leading edge. The drag force acting on the portion of ice that is still fixed to the leading edge creates a boundary condition. The ice which has slid past the tip has a free boundary condition and the drag acting on it creates a bending moment due to the distributed shear load. This directly leads to the hypothesis that either the bending moment causes a direct tensile strength failure, or a direct transverse shear strength failure.
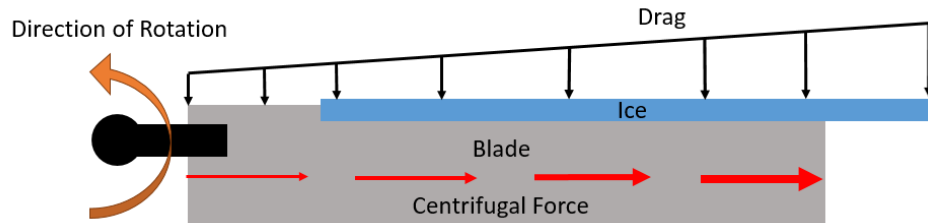
Figure 2.2. Top View Diagram of Blade with Ice During Shedding

2.1.2 Assumptions

From the schematic shown in Figure 2.2, several assumptions can be made to model the ice fracture as a beam bending problem. The portion of ice that has not slide past the tip of the blade is being held against the leading edge by the drag force, and can be simulated as a clamped boundary condition. The portion of ice which has slid past the tip is still subjected to a drag force and has nothing to prevent it from bending. This condition can be modeled as a free boundary condition. Using these boundary condition assumptions, the overhanging ice can be modeled as a cantilever beam. As the ice slides past the tip of the blade, it breaks into small pieces that were experimentally measured to be approximately 4 inches long. The span-wise velocity increase over 4 inches is 3.7 m/s which in turn results in a drag force increase of 10 N. These increases will have a negligible effect on the predicted failure length and therefore it can be assumed that the velocity is constant and will be equal to the tip speed of the rotor blade. Consequently, this also allows the drag force to be assumed constant across the ice beam. Lastly, the cross-section of the ice shape could be assumed to be symmetric, resembling a "C" or semi-circle shape. A symmetric cross-section significantly simplifies the beam bending equation by reducing the number of second moments of area that need to be determined. The "C", or semi-circle, shape assumption eliminates the need to determine the drag coefficient, C_d, experimentally, and instead the known value of 1.2 can be used [36]. An experiment to model summary of these assumptions can be seen in Figure 2.3.
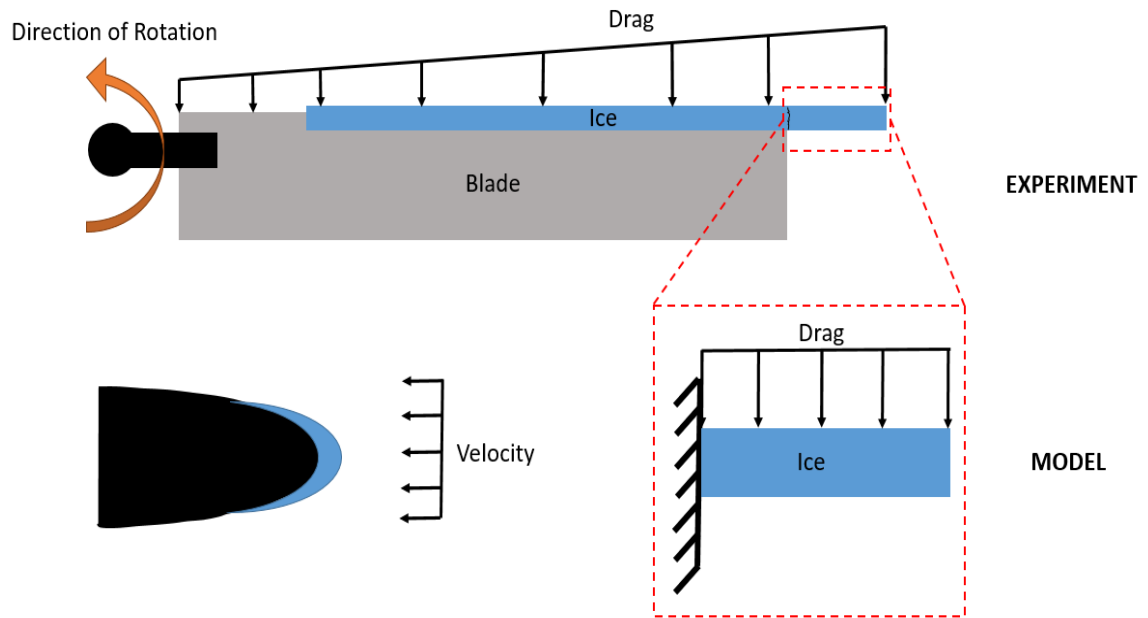
Figure 2.3. Top View Diagram of Experiment and Simplified Model Diagram

2.2 Euler Bernoulli vs. Timoshenko

When formulating a failure model responsible for ice fracture, the short length of the ice beams needs to be taken into account. Shorter beams could fail due to a transverse shear stress rather than by a tensile stress. An Euler-Bernoulli approach is used to evaluate the failure lengths due to a tensile stress and a Timoshenko approach is used for failure by a transverse shear stress.

2.2.1 Euler-Bernoulli Approach

The first approach uses an Euler-Bernoulli model to determine the projectile length due to direct tensile stress failure associated with the bending moment created by the drag force. Using the assumptions stated in the above section, a bending stress equation can be derived from Euler-Bernoulli beam theory.

The bending moment is a result of the drag force which is a function of velocity. The span-wise velocity of the overhanging ice shape is assumed to be constant and equal to the tip speed of the blade. Since the rotational speed of the rotor shaft is known, the velocity, v, can be calculated using Equation 2.1 and is equal to the rotational speed of the rotor shaft, Ω, multiplied by the radial distance from the center of the hub to the tip of the blade, R.

$$v = \Omega * R \tag{2.1}$$

Once the velocity of the tip of the blade is known, the drag, D, can be calculated using Equation 2.2. In this equation D is the drag force, ρ is the density of air at -14°C (1.29 kg/m³), C_d is the section coefficient of drag and is equal to 1.2, and *chord* is the horizontal distance from the leading edge to the trailing edge of the ice shape.

$$drag = \frac{1}{2}\rho v^2 C_d chord \tag{2.2}$$

Finally, the bending moment, M, can be calculated. A moment is defined as the cross product between force and distance, however the drag force is acting as a constant uniform load over the length of the ice beam. Therefore, M must be calculated by integrating the drag force over the entire length of the ice beam as shown in Equation 2.3. The result is the bending moment is equal to half of the drag force multiplied by the squared length of the ice beam.

$$M = \int_0^l drag * xdx = \frac{1}{2}drag * l^2 \tag{2.3}$$

By assuming that the cross-section of the ice shapes are symmetric, the bending

stress equation derived from Euler-Bernoulli beam theory is described by Equation 2.4. The bending stress is found to be equal to M (the bending moment), multiplied by c (the distance from the centroid to the leading edge where the point of maximum tension occurs), and divided by I (the second moment of area about the bending axis).

$$\sigma = \frac{Mc}{I} \tag{2.4}$$

2.2.2 Timoshenko Approach

The second approach investigated the ice projectile length due to direct transverse shear stress failure associated with the shear force created by the drag force. Using the assumptions from the "Assumptions" section, the transverse shear stress equation, derived using Timoshenko beam theory, can be simplified. This section will go through a brief derivation of the transverse shear stress equation. A full derivation of Timoshenko's equations can be found in Wang et al. [37].

The transverse shear stress due to a lateral load is shown in Equation 2.5 below. It is equal to the modulus of rigidity, G, times the square of the shear correction factor, k, multiplied by the quantity containing the sum of the rotation of the cross-section as function of x, $\phi(x)$, and the derivative with respect to the x direction of the Timoshenko derived beam deflection, $w_0^T(x)$. To make use of this equation, the rotation of the cross-section and the derivative of the lateral deflection using Euler-Bernoulli assumptions must be found.

$$\sigma_{xz}(x) = G * k^2 * (\phi(x) + \frac{dw_0^T(x)}{dx}) \tag{2.5}$$

The rotation of the ice beam cross-section as a function of x for a clamped-free beam is equal to the negative derivative of the lateral deflection with respect to x using an Euler-Bernoulli derived equation and is shown in Equation 2.6 below.

$$\phi(x) = -\frac{dw_0^E(x)}{dx} \tag{2.6}$$

For a uniformly distributed load along a clamped-free beam the derivative of the equation for deflection under Euler-Bernoulli assumptions is given in Equation 2.7. Where q_0 is the uniform distributed load, L is the length of the beam, and EI is the flexural rigidity.

$$\frac{dw_0^E(x)}{dx} = \frac{q_0 L^2}{6EI}(3x - 3\frac{x^2}{L} + \frac{x^3}{L^2}) \tag{2.7}$$

For a clamped-free beam under a uniformly distributed load the Timoshenko lateral deflection equation is given in Equation 2.8 and its derivative is given in Equation 2.9.

$$w_0^T(x) = \frac{q_0 L^4}{24EI}(6\frac{x^2}{L^2} - 4\frac{x^3}{L^3} + \frac{x^4}{L^4}) + \frac{q_0 L^2}{2kGA}\frac{x}{L}(2 - \frac{x}{L}) \tag{2.8}$$

$$\frac{dw_0^T(x)}{dx} = \frac{q_0 L^2}{6EI}(3x - 3\frac{x^2}{L} + \frac{x^3}{L^2}) + \frac{q_0 L}{kGA}(1 - \frac{x}{L}) \tag{2.9}$$

Substituting Equation 2.7 into Equation 2.6 and then substituting this along with Equation 2.9 into Equation 2.5 yields the final form of the Equation for the transverse shear stress, shown in Equation 2.10. Evaluating this expression at $x=0$ yields the maximum transverse shear stress.

$$\sigma_{xz}(x) = \frac{Drag * k * L}{A}(1 - \frac{x}{L}) \tag{2.10}$$

It is also interesting to verify that deriving an expression for the bending stress using Timoshenko's assumptions yields the same equation that was derived using Euler-Bernoulli assumptions.

2.2.3 Model Comparison

The models were compared to determine which would be selected to develop a prediction tool for projectile lengths. The Euler-Bernoulli bending stress model becomes the obvious choice after taking into account several key points.

First, the transverse shear strength model is dependent upon knowing the shear correction factor, k. Determining this correction factor for complex geometry such as an ice shape is not trivial. A numerical finite element method using three dimensional linear elasticity would be needed to most accurately determine the correction factor. Other methods to determine shear stresses on the beams would divide the average shear strain of an ice section by the shear strain at the centroid. In either case this is time consuming.

Second, the ultimate shear strength of impact ice (which is needed to compare to the stress created by the shear force for failure) is unknown. The ultimate tensile strength of impact ice (which is needed to compare the bending model to for failure) is also unknown, but it is simpler in practice to determine experimentally than the ultimate shear strength. Von Mises criterion can be used to approximate the ultimate shear strength to be 57.7% of the ultimate tensile strength, but further assumptions are introduced in the model. The approximations and assumptions used, coupled with the lack of a known shear correction factor for the ice shapes creates a large source of uncertainty within the model if implementing Timoshenko approaches.

Despite the shortcomings related to the prediction of shear stress in the ice beam, the Timoshenko model was run using experimental cross-sectional properties and the predicted projectile lengths were compared to experimental results. The ultimate shear strength used for failure analysis was half the experimentally determined ultimate tensile strength. The shear correction factor was set equal to 1 to predict the largest possible shear stress. The transverse shear strength model predicted projectile lengths over 1m long. Lowering the correction factor to 0.1 only increased the projectile length. For this reason along with the large uncertainty in the shear failure strength and correction factor, the transverse shear model is rejected and the bending stress model is explored in detail.

2.3 Corrections to the Euler-Bernoulli Model

2.3.1 Non-Symmetric Ice Shape Correction

After collection of the experimental data including: projectile lengths, cross-sectional ice shape properties, and pictures of the ice beam cross-sections, a key correction needed to be made to the Euler-Bernoulli bending stress model. It was previously assumed that the cross-sectional ice shapes would be symmetric about an axis. A raw photograph of an ice shape is shown in Figure 2.4 and a digitized rotated version of the same ice shape is shown in Figure 2.5.
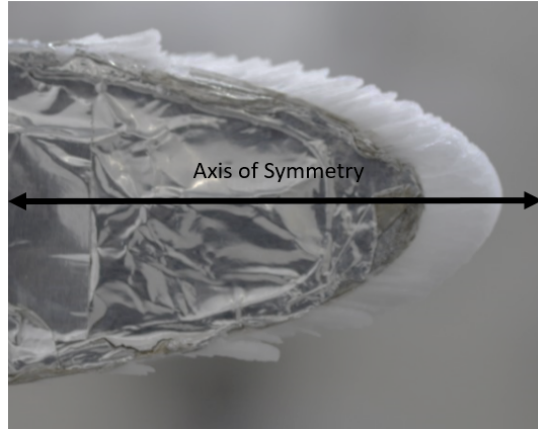
Figure 2.4. 5 Minute Accretion Test 2 Cross Sectional View of Ice Shape Photographed on Rotor Blade
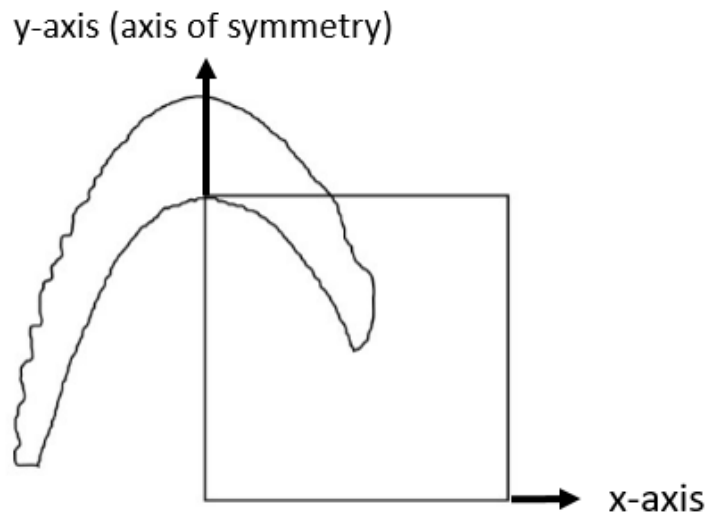
Figure 2.5. 5 Minute Accretion Test 2 Cross Sectional View of Digitized Ice Shape with 1in x 1in Calibration Square

As seen in these two Figures, the cross-sectional ice shape is not symmetric. The bending stress needs to be corrected to account for the lack of symmetry. This involves re-deriving the bending stress equation to account for the contributions of all 3 second moment of areas, I_{xx}, I_{yy}, and I_{xy}. Defining a coordinate axis with y in the vertical direction and x in the horizontal direction, the bending moment due to the drag force will be about the x axis. There will be no y or z bending

moment contributions. This allows effective bending moments in x, $\bar{M}_x$ (Equation 2.11), and y, $\bar{M}_y$ (Equation 2.12) to be derived and simplified.

$$\bar{M}_x = \frac{Drag}{1 - \frac{I_{xy}^2}{I_{xx}I_{yy}}} \tag{2.11}$$

$$\bar{M}_y = -\frac{\frac{Drag * I_{xy}}{I_{xx}}}{1 - \frac{I_{xy}^2}{I_{xx}I_{yy}}} \tag{2.12}$$

Substitution of these two equations into Equation 2.13 yields the bending equation for non-symmetric ice beam cross-sections. Where $\bar{y}$ and $\bar{x}$ are the y and x distances, respectively, from the centroid to the location of the maximum tensile stress, and I_{xx}, I_{yy}, and I_{xy} are the second moment of areas about the x axis, y axis and x-y plane respectively.

$$\sigma_{bend} = \frac{\bar{M}_x}{I_{xx}}\bar{y} + \frac{\bar{M}_y}{I_{yy}}\bar{x} \tag{2.13}$$

Chapter 3 |

Facility Overview and Experimental Test Configuration

3.1 Facility Overview

The Pennsylvania State University's Adverse Environment Rotor Test Stand (AERTS) facility was used to perform experiments to achieve the goals laid out in Chapter 1. This section discusses the capabilities of the facility, improvements made to improve the accuracy of the experimental measurements, and instruments used in the experiment.

3.1.1 AERTS Capabilities

AERTS is a state-of-the-art facility for icing testing of truncated helicopter blades, propellers, and wind turbine blades. In addition, the facility is used to conduct significant research on ice adhesion strength for various ice protective coatings. The rotor stand, shown in Figure 3.1, consists of a QH-50 rotor hub, a 125 horsepower motor, and linear actuators to control collective and lateral pitch.

The stand can be connected to four slip rings which carry 48 signal channels and 24 power channels from the rotating frame of the rotor to the fixed frame control room. The slip rings are used to transfer electronic sensor signals as well as electrical equipment power to the rotor blades, allowing for testing of de-icing systems. The stand is enclosed by a ballistic wall and is contained in a 19.7 ft (6 m)x 19.7 ft (6 m) x 11.5 ft (3.5 m) commercial freezer, shown in Figure 3.2.
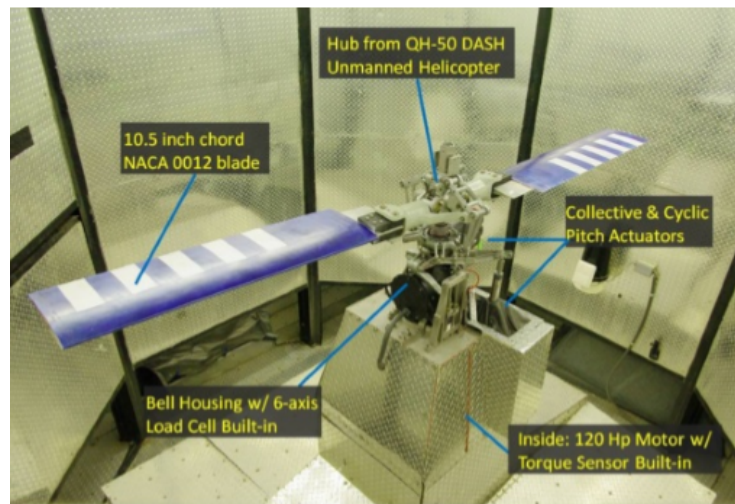
Figure 3.1. Rotor Stand Schematic [4]
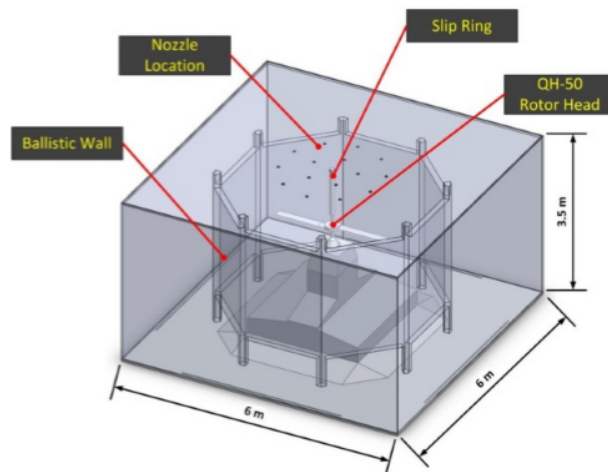
Figure 3.2. AERTS Facility Diagram [4]

Located above the rotor test stand and in the ceiling of the freezer are two concentric rings of NASA standard atomizing nozzles. The inner ring contains five nozzles, while the outer ring contains 10 nozzles. These nozzles can be used in any combination based on the test configuration. Typically, the outer ring of nozzles is used with either the even nozzles turned on or the odd nozzles turned on.

The facility is capable of accommodating blades up to 9.8 ft (3 m) in diameter, limited due to the geometry of the ballistic wall, and can spin them at speeds up to 1500 RPM. The freezer allows for the test temperature to be varied between ambient and -25°C. The MVD of the water droplets can be varied between 10 and 50 microns. The LWC of the cloud is not directly controlled, and is a function of the number of nozzles used and the input pressure to those nozzles. LWC is measured after performing a test.

3.1.1.1   Improved Nozzle Housing

A major assumption made prior to performing any experiments is that ice accretion on the leading edge of the blades would be linear, with the largest amount of accretion at the tip and the least amount at the root. During initial testing, it was noticed that the icing cloud was not mixing properly and as such, the ice was not accreting linearly. Most of the ice accretion was concentrated at the $\frac{3}{4}$ span of the rotor, right under the location of the icing nozzles. The main reason for the lack of linear ice accretion was due to the icing cloud not uniformly mixing because the collective pitch angle of the rotor was approximately 0°. The 0° collective pitch angle was selected to ensure that the forces acting on the overhanging ice were related to drag forces only, simplifying the model. To enhance mixing of the cloud and achieve linear accretion of ice along the leading edge of the blade, the plume of the nozzles needed to be controlled such that it can be directed along the span of

the blade.

In the original configuration, the nozzle housing is bolted outside of the freezer to the ceiling, which allows the nozzles themselves to be accessible from inside of the freezer. As shown in Figure 3.3, the nozzles are almost flush with the inside ceiling, are pointed directly downwards (located at the $\frac{3}{4}$ span of the used rotor), and are unable to move. To gain control of the nozzle plume and enhance mixing of the cloud, four of the nozzle housings on the outer ring were modified to pivot back and forth along the span of the blade.

Figure 3.3. Old Nozzle Housing and Configuration

The rotation of the nozzles was accomplished by first dropping the nozzle housings 2 inches (5.1 cm) from the top of the ceiling into the chamber. A face plate was then attached to the bottom of the housing and attached to either side of the face plate were two struts. The struts were then bolted to a ring which was bolted into the ceiling of the freezer. The bolts connecting the struts to the ring can be loosened, allowing the nozzle to pivot. Once the nozzle is in the desired

position, these bolts can be tightened to lock it in place. A simplified schematic and a picture of the new nozzle housing can be seen in Figure 3.4. By directing two nozzles downward, one toward the blades tips, and one towards the root, the icing cloud mixed uniformly. The result was the linear accretion of ice from the blade tip to root that was assumed prior to testing.
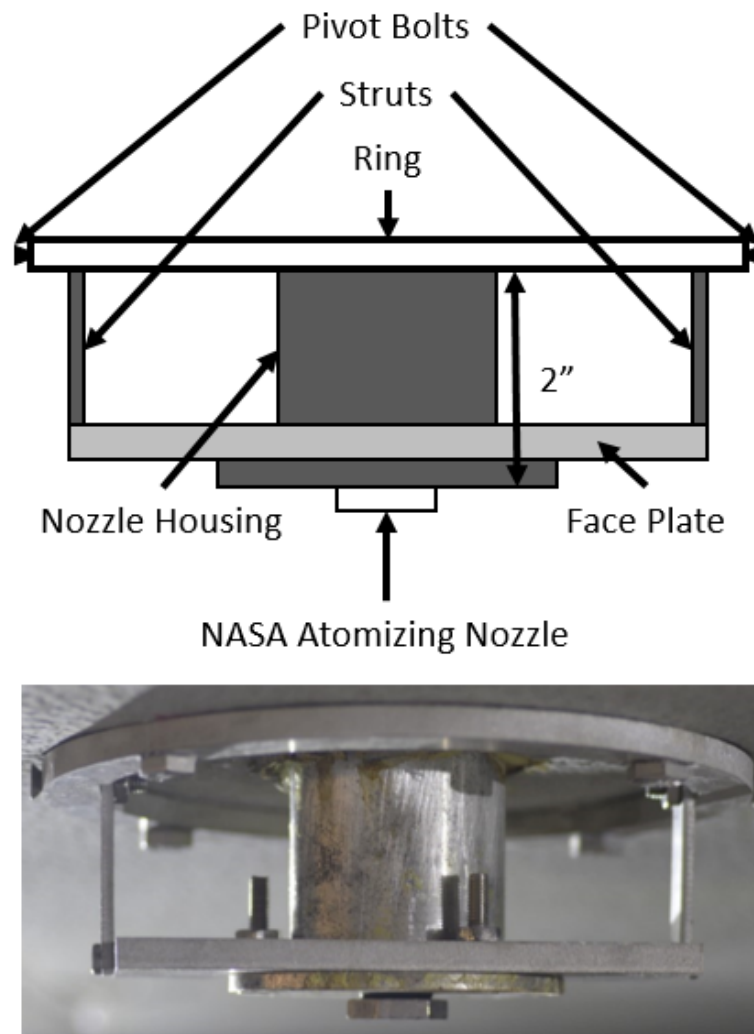
Figure 3.4. Schematic and Picture of Improved Nozzle Housing and Configuration

3.1.2 Blades

Two NACA 0012 rotor blades were used in this experiment. The NACA 0012 airfoil is a symmetric airfoil and therefore has no camber. The blades were cut to lengths of 56 in (1.42 m), with the chord measuring 9.5 in (24.13 cm) at the tip and 11.5 in (29.21 cm) at the root. The blades were modified to include an inboard and outboard electro-thermal deicing system. The de-icing systems are formed by proprietary heatable paint developed by Villinger R&D.

3.1.2.1   Heaters

The blades have different inboard and outboard heating zone designs, each dedicated to specific data collection requirements. Blade one, shown in Figure 3.5, was designed to mimic an actual de-icing system on a helicopter blade and was the blade used for shedding ice during rotation. The heating zone was limited to the leading edge area of the blade and covers a total surface area of 1980 cm^2 (306.9 in^2). The power density of the heaters are 1.3 W/cm^2 (8.39 W/in^2).
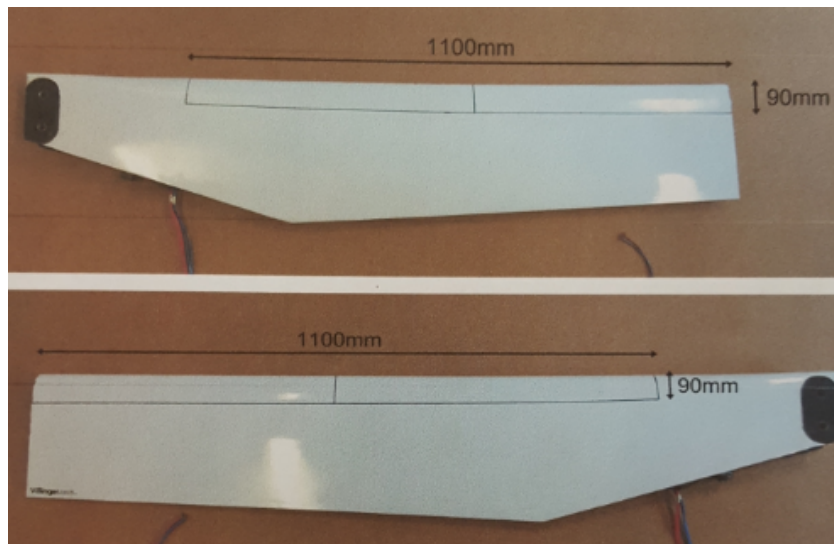
Figure 3.5. Heater Dimensions of the Top and Bottom Sides of Blade One

Blade two, shown in Figure 3.6, was designed to remove accreted ice from the blade while the rotor was stopped. A single large beam of ice is removed manually from the rotor assisted by the melting of the ice interface using the heaters. This beam of ice would then be used in the beam bending experiment for determination of the ultimate tensile strength of impact ice. In addition, this beam of ice was also cut using a hot plate to estimate the cross-sectional area properties of the ice past the tip, allowing a better model prediction for ice projectiles shed after the first projectile. This procedure is described in detail later in this chapter. The heating zone covers a surface area of 3690 cm^2 (571.95 in^2) and has a power density of 0.73 W/cm^2 (4.71 W/in^2).
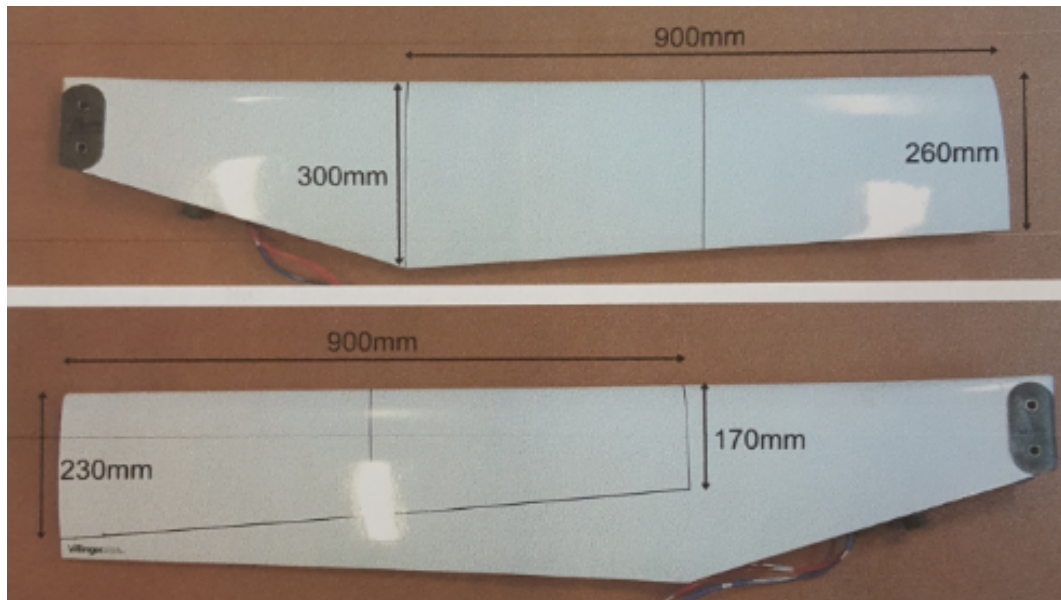
Figure 3.6. Heater Dimensions of the Top and Bottom Sides of Blade Two

The power wires for each heating element were split to have 3 redundant hot wires and 3 redundant cold wires. This was done purely for safety in the event one of the wires lost contact during rotation, was cut, or became disconnected from the circuit. As previously said, the slip ring was used to provide the necessary power

to run the heaters. Since each blade has 2 heating elements, all 24 power channels on the slip ring were used.

3.2 Test Matrix

3.2.1 Ice Projectile Length

Testing for the ice projectile length was conducted at representative in-flight icing conditions. The test temperature, MVD, and air pressure to the nozzles in the AERTS facility was controlled using an in house LabVIEW code. The front panel of the LabVIEW code can be seen in Figure 3.7. LabVIEW, Laboratory Vitrual Instrument Engineering Workbench, is a visual programming language developed by National Instruments. It is most commonly used for data acquisition, instrument control, and automation.

These tests were run on the 20 psi airline The test temperature was set at -14°C, MVD was set to 20 microns, the rotor was operated at 350 RPM, and the LWC was measured to be 0.8 g/m^3 (+/-30%). The length of accretion time was varied to determine if the projectile lengths were functions of the cross-sectional area properties. Tests were ran at both 3 minutes of accretion time and at 5 minutes.
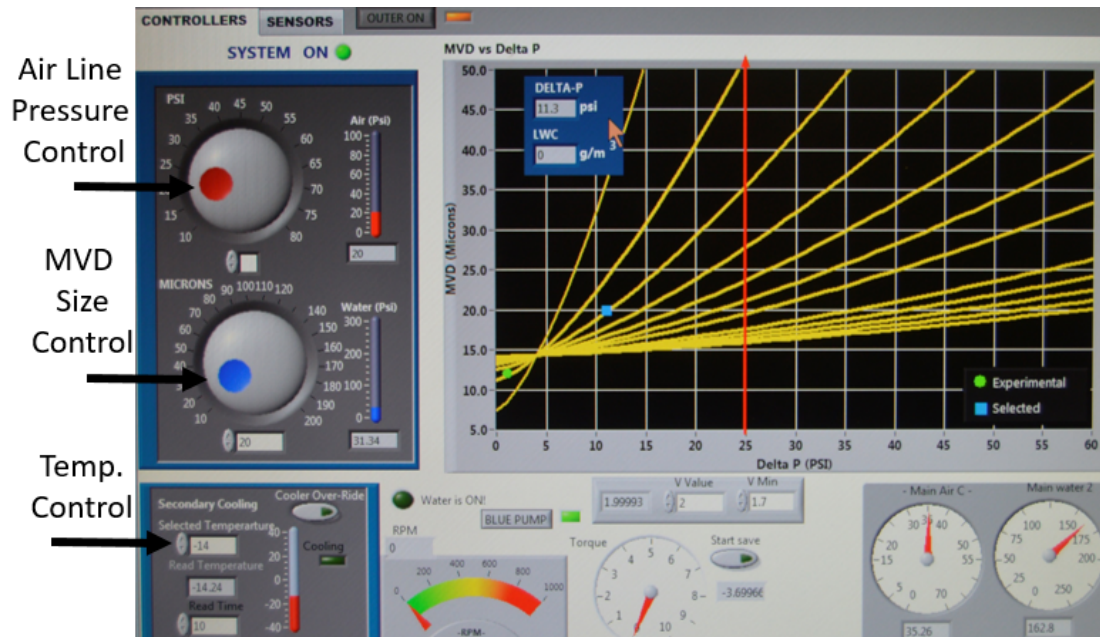
Figure 3.7. Front Panel of LabVIEW Code for AERTS Facility Controls

3.2.2 Ultimate Tensile Strength

Testing for the ultimate tensile strength of ice was also conducted at the same representative in-flight icing conditions. As stated in the above section, all of the test parameters for the icing cloud were controlled using LabVIEW, reference Figure 3.7. The test temperature was -14°C, MVD was 20 microns, the rotor shaft speed was 350 RPM, and the LWC was measured to be 0.8 g/m³ (+/-30%). It was necessary to determine whether the thickness of the ice was a function of the ultimate tensile strength. This meant varying either LWC or the accretion time. Since accretion time is significantly easier to control this was the parameter varied. The accretion test time was varied between 3 and 5 minutes.

3.3 Experimental Measurement Procedures

Verification of the Euler-Bernoulli model devloped in Chapter 2 requires the experimental cross-sectional properties of the ice shapes as well as experimental projectile lengths to compare the model to. In addition, the model requires the ultimate tensile strength of ice and a secondary goal of finding this value experimentally was also defined at the conclusion Chapter 1. The experimental ice shape cross-sectional properties, ultimate tensile strength measurements, and the experimental ice projectile length measurements will each have a unique procedure described in this section.

3.3.1 Ice Projectile Length Measurements

3.3.1.1 High-Speed Cameras

Two Phantom MIO 310 series high-speed cameras were utilized to visualize the ice shed event. Both have a resolution of 1280x800 pixels and are capable of capturing 3000 frames per second (fps). The only difference between the two cameras is that one is gray scale and the other is color. A 35 mm wide angle lens was attached to each camera in order to maximize the field of view. The cameras were positioned on top of the ballistic wall opposite of each other and aimed down over the rotor plane. One camera looked down the left side of the rotor and the other looked down the right side. A top view of the camera placement can be seen in Figure 3.8. This configuration allowed the cameras to cover a majority of the rotor plane and maximizes the chances of capturing the shedding event. A 500W hydrargyrum medium-arc iodide (HMI) light was positioned along the top of the ballistic wall near camera one and was pointed down over the rotor plane in such a

way that camera one's field of view was illuminated. Three light emitting diode (LED) arrays were positioned along the top of the ballistic wall around camera two and were aimed down over the rotor plane such that camera two's field of view was illuminated. The lights were necessary for two reasons. First, the lighting in the facility is relatively poor at cold temperatures. Second, the high-speed cameras have an extremely short exposure time compared to a normal digital camera. This increases the light requirement to clearly capture high-speed images.
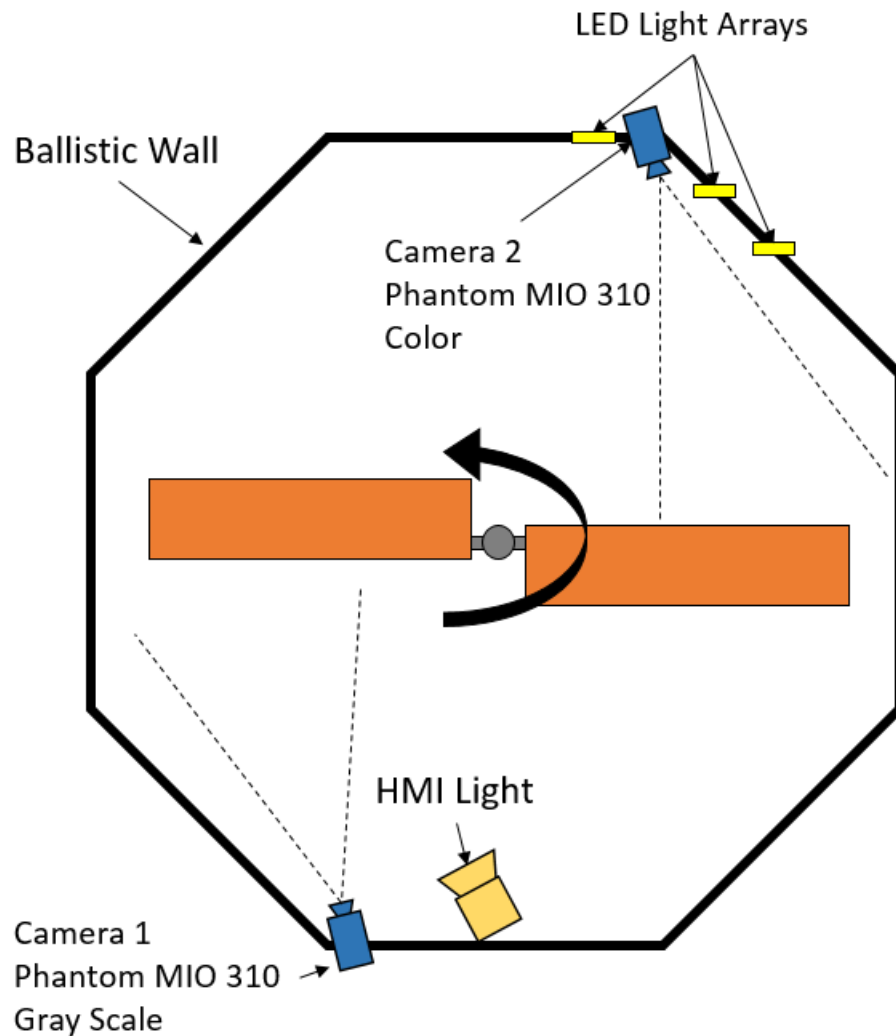
Figure 3.8. Top View of High-Speed Camera and Lighting Placement

The backs of the cameras have two bayonet Neill-Concelman (BNC) connector posts. One of the posts is labeled "trigger" and is used to manually trigger the camera to collect data. The other post is labeled "fsync" and is used when there is a need for a master and a slave camera. For the purpose of this experiment it was necessary to manually trigger both cameras to collect data at the same time. To accomplish this, a BNC coaxial cable was connected to the "trigger" post on each camera. These BNC cables were then run to a BNC T connector. From the bottom post of the T connector, a 3rd BNC cable was run to a single pole switch. This switch was used to manually trigger the cameras to collect data. Before the switch for manual triggering could be used, the cameras needed to be synced with one another. To do this a master camera needed to be selected in the camera software. For this experiment, camera one (the gray-scale) was selected as the master, and camera two the slave. To identify camera two as a slave, the IP address of camera was inputted in the master camera text box in the menu for camera two. Finally, a BNC cable was connected between the fsync ports on both cameras. Once the slave camera was synced with the master, both could then be manually triggered by throwing the single pole switch. A schematic of this wiring configuration is shown in Figure 3.9 below.
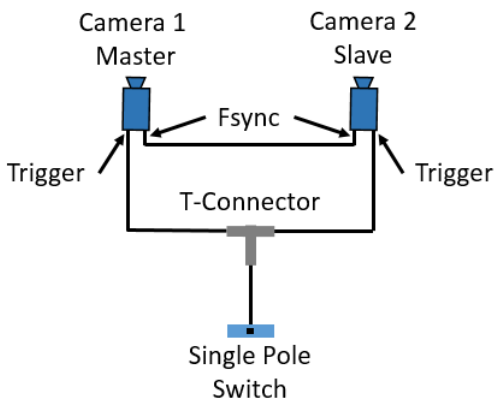
Figure 3.9. Schematic of Wiring For High-Speed Camera Triggering and Syncing

3.3.1.2 Procedure

Upon reaching the preselected duration of ice accretion, the rotor was stopped and the cross-section of the ice shape on the tip of the shed blade was photographed using a high resolution camera with a macro lens. The photograph is necessary to determine the cross-sectional properties of the ice beam. The procedure to acquire such properties and an example photograph is presented in the next section. Once the photographs were taken, the rotor was spun back up to 350 RPM. Upon reaching 350 RPM, the de-icing system on blade one was activated using an in house LabVIEW code. A picture of the codes front panel is shown in Figure 3.10.
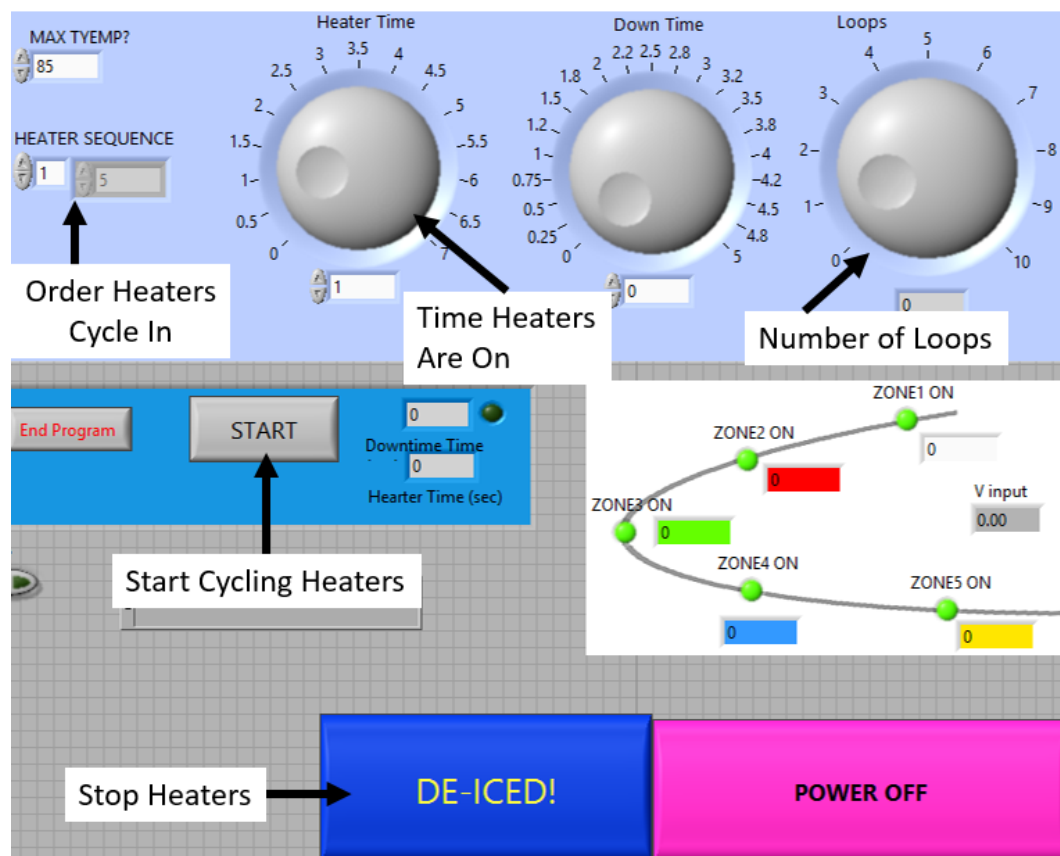
Figure 3.10. Front Panel of Heater LabVIEW Code

Two relays were used in conjunction with the code, with one relay connected to the inboard heater and the other connected to the outboard heater. These relays controlled when power was sent through the slip ring to power the heaters. They were controlled by the LabVIEW code. To mimic an actual in-flight de-icing system, the code was set to cycle the heaters inboard to outboard at two seconds of heat each. The cycle was repeated until the ice shed. The high-speed cameras were triggered simultaneously when an audible noise of the shed ice hitting the ballistic wall was heard. The triggering of the cameras recorded the previous three seconds of images, capturing the shedding event. Once a shedding event has been recorded, the video was reviewed and a stack of images showing the shedding event was saved for processing. A typical image contained main ice projectiles for quantification of the ice projectile length, as well as a cloud of broken feathers which are ignored. An example of an image used for processing can be seen in Figure 3.11.
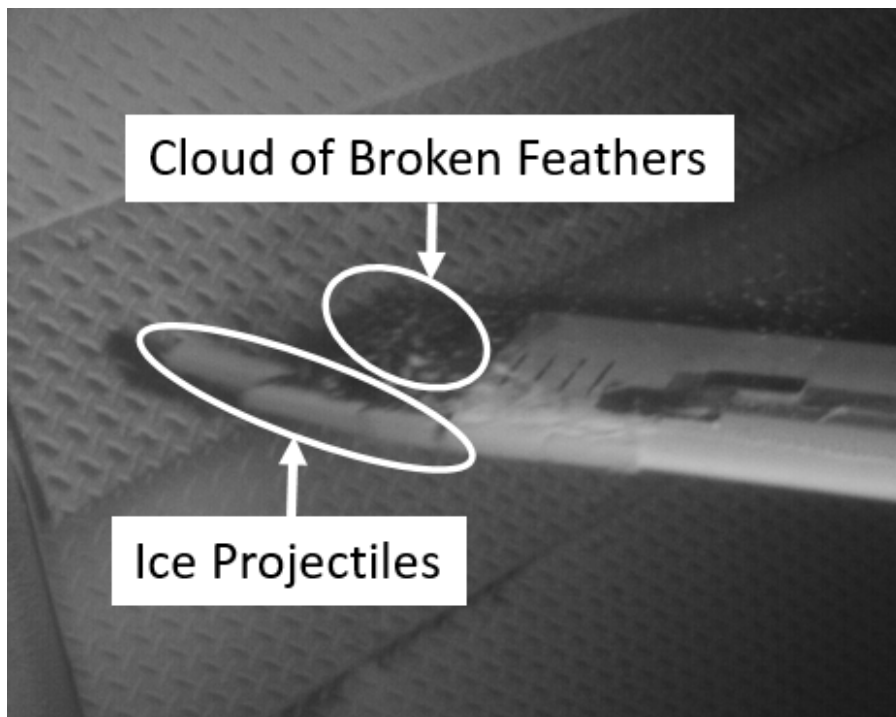
Figure 3.11. Example of High-Speed Video Image of Shedding Event

The projectile lengths were then determined using a program known as ImageJ. ImageJ is a Java-based image processing program developed by National Institutes of Health, typically used for image processing and analysis. The program is open source so many user-written plugins are available to extend its utility.

First, an image such as the one in Figure 3.12 is imported into ImageJ. Next, the amount of pixels per unit length was calibrated based on reference geometry. The calibration was accomplished by first drawing a line using the line tool in ImageJ between the 4 black stripes at the tip of the shed blade, shown in Figure 3.12 and shown in greater detail in 3.13. Once a line has been drawn, the set scale feature was used. The first box in the pop-up menu displayed the known distance in pixels of the line drawn. In the second box, input the known distance for calibration of 3.5 in (8.9 cm). The known distance was referenced from the geometry between the drawn lines on the rotor blade. The last two boxes are left alone and the output scaling, given in pixels/unit (where unit in this case is inches), was recorded. The line tool was used again to measure the length of the ice projectile in that particular photograph, shown in Figure 3.12. This process was repeated for each photograph containing ice projectiles.
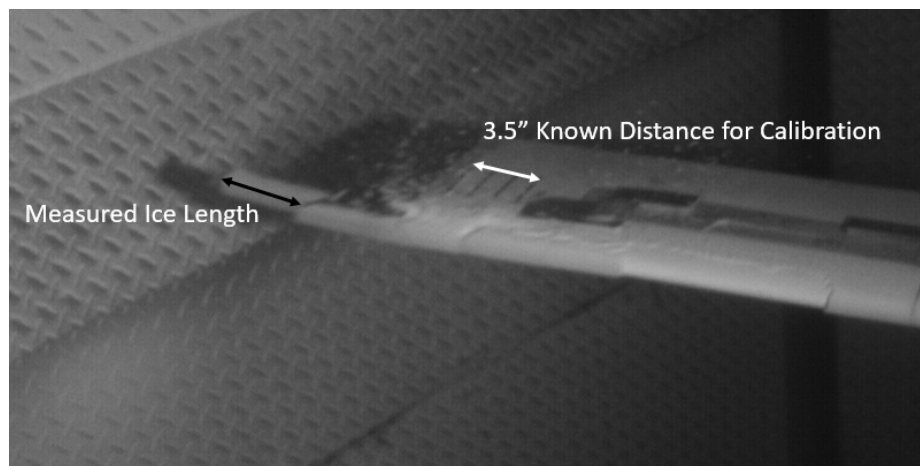
Figure 3.12. Example Photograph of Ice Projectile Quantified using ImageJ
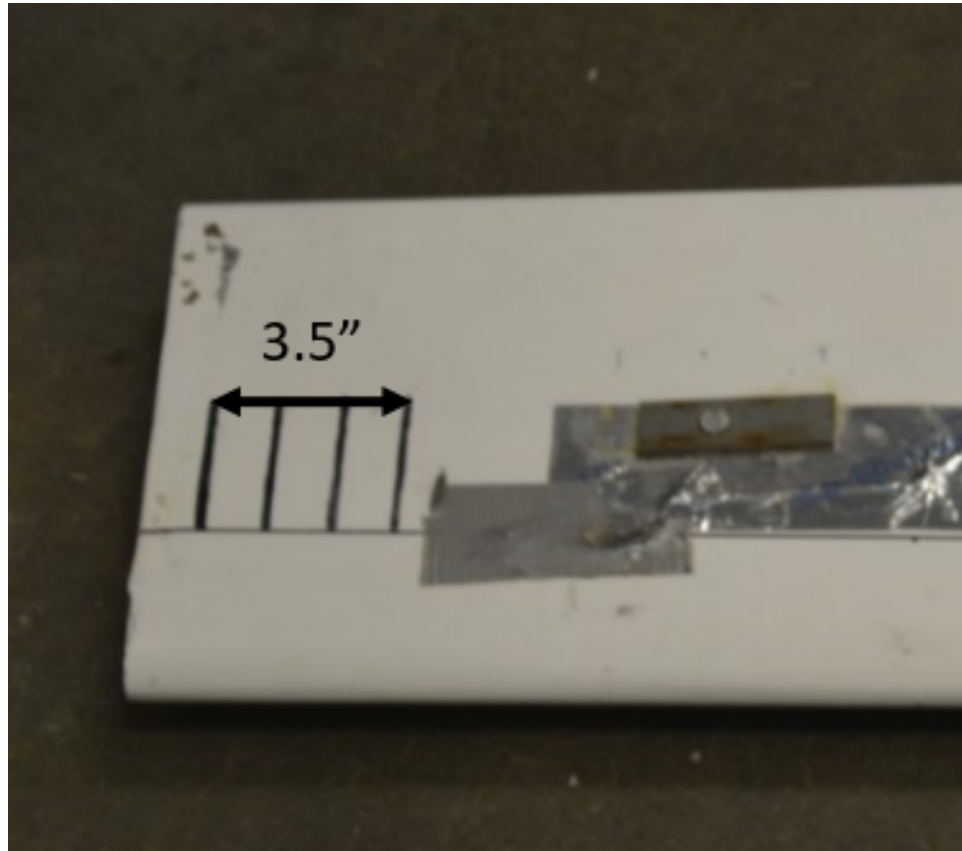
Figure 3.13. Known Distance Measurement for Calibration of Ice Projectile Photos on Shedding Blade

If there were multiple ice projectiles during a given shedding event, the ice beam on the non-shedding blade (blade two) was analyzed for variation in the cross-sectional area properties, instead of being used for the ultimate tensile stress test. To determine the variation in the cross-sectional area properties, the ice beam was removed from the blade in one long piece, accomplished using the same process to remove ice beams as described in the "Ultimate Tensile Strength" section below. Once removed, the ice was cut (starting at the tip) every 4in (10.16 cm) using a hot plate and photographs were taken of the cross-sections and processed using the same process as described in the "Ice Shape Cross-Sectional Properties" section. Knowing the cross-sectional area properties across a majority of the leading

edge allows a better model prediction for the lengths of ice projectiles because the properties at a location closer to the break face can be used. It is important to note that this can be done since it is assumed that ice accretion is uniform along the leading edge of both blades.

3.3.2 Ice Shape Cross-Sectional Properties

The ice shapes accreted on the rotor blades have complex geometry. There is no simple way to calculate the needed cross-sectional properties. A procedure was developed to determine the relevant properties using digitized cross-sectional ice shapes and computer software.

3.3.2.1 Digital Camera and Digital Flash

A Nikon D500 digital single-lens reflex (DSLR) camera was used to photograph the cross-sections of the ice shapes. A 60mm Nikon macro lens with manual aperture control was attached to the camera. This lens was selected to allow close up high resolution photographs to be taken. A Nikon SB-700 AF Speedlight digital flash was also used. The Speedlight flash was necessary due to the poor lighting conditions of the walk in freezer and the flash on the digital camera being insufficient for the quality of photographs required.

3.3.2.2 Procedure

After ice has been accreted on the shedding rotor blade, or an ice beam was broken (process described in the next section), a high-resolution picture was taken using the digital camera and flash. For the shedding tests this picture was of the cross-section of the ice at the tip of the shedding blade and for the beam

bending test this picture was of the cross-section of the break face of the ice. For the shedding tests, a piece of engineering grid paper was taped to the tip of the blade for image calibration purposes, as shown in Figure 3.14. For both the beam bending test conducted to measure the ultimate direct stress of the ice shape, and determination of the variation in the ice cross-sectional area properties, the ice was placed on a box with the break face parallel with the box's edge. A piece of engineering grid paper was attached to the box and used for image calibration purposes, shown in Figure 3.15.
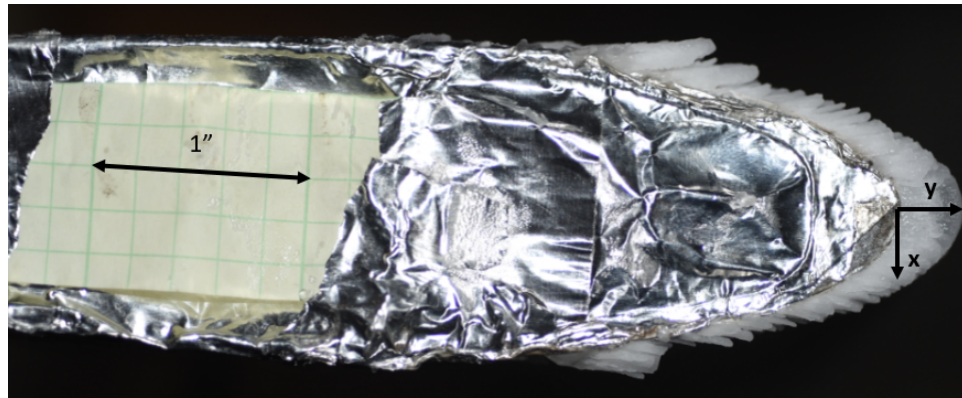
Figure 3.14. Shedding 3 Minute Test 1 Ice Shape on the Tip of Shedding Blade with Grid Paper for Calibration
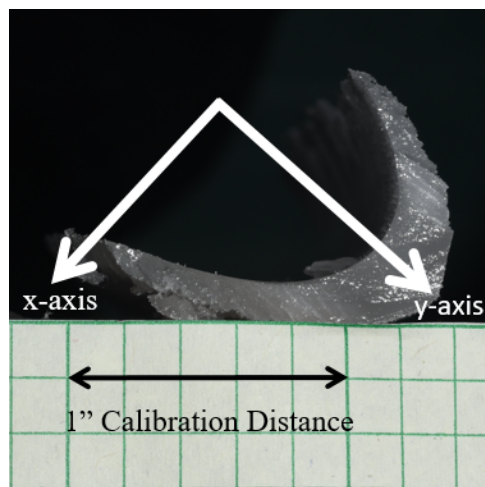
Figure 3.15. Beam Bending 3 Minute Test 1 Ice Shape with Grid Paper for Calibration

Using Adobe Photoshop, the pictures were first rotated until the x-y axis was normally oriented such that the y-axis was vertical and the x-axis was horizontal and both are pointing in the standard positive directions. Next, the cross-section of the ice shape, exclusively, was extracted using the quick select tool, converted into a path, and then into a shape. Converting the extracted ice shape into a shape allowed it to have its own layer, which was separate from the rest of the picture. This was useful in the coming steps. Next, the ruler tool is used to measure the amount of pixels between the 1 in (2.54 cm) known calibration distance. Once the number of pixels per one inch in the picture was known, a one inch by one inch calibration square was created using the rectangle tool and inputting x pixels by x pixels (where x is the number of pixels per inch). Finally, the layer containing the original picture was turned off, leaving just the ice shape cross-section and the calibration square. An example of what this looks like is shown in Figure 3.16. This image was saved and used for digitization in the next steps.
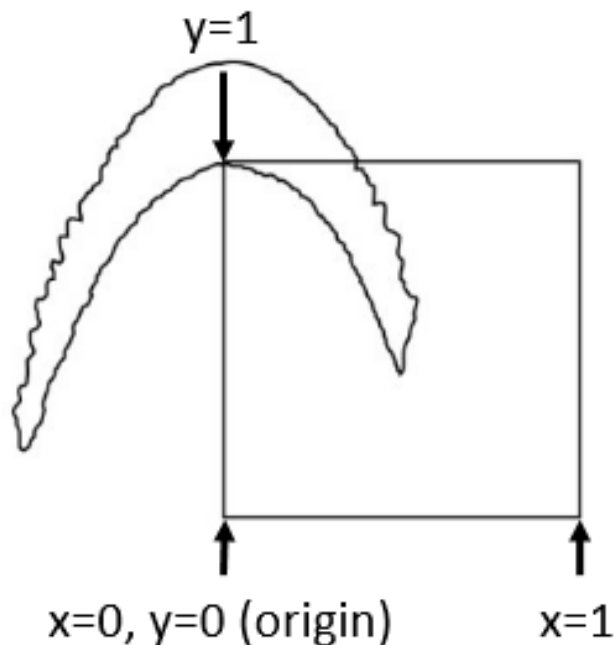
Figure 3.16. 3 Minute Test 1 Ice Shape and 1x1 Calibration Square Photoshop Result

The processed images created in Adobe Photoshop were next imported into a program called GetData Graph Digitizer. This program converted the curvature of the ice shape into an x and y coordinate sheet. First, the set scale tool was used to set the origin (x=0, y=0) at the bottom left corner of the calibration square, x=1 at the bottom right corner of the square, and y=1 at the top left corner of the square. Next, the digitize area tool was used to populate the ice shape with data points and the reorder tool was used to put the points in numerical order around the ice shape. Once the data points were in order around the ice shape (either counter-clockwise or clockwise), the export data tool was used to export the data points to a text file containing scaled x-y coordinates. To finish preparing the text file for the final steps, a third column was added for the z-coordinates. Since the shape is only a 2-D shape in x and y, this needed to be a column of zeros. The easiest way to do this was to copy the x-y coordinates into an excel file, add the column of zeros, and then export this excel file to a tab de-limited text file.

To complete the final steps and acquire the cross-sectional area properties of the ice shape, a 3D modeling program called SolidWorks was used. The process was initiated by creating a new part file. Next, it was important to make sure the units the program was working in were English units (inch, lb etc.). The units the program was working in could be checked by opening the options menu, clicking document properties, opening the units tab, and selecting the "IPS" option. Now the final text file of x-y-z coordinates created in the above steps can be imported into SolidWorks using the curve through x-y-z coordinates tool. The tool essentially takes the x-y-z coordinates and draws a spline between each point. If the points are not ordered either counter-clockwise or clockwise, the tool will either fail to import the shape or the shape drawn will not resemble the ice shape. Next, the sketch tool needed to be used to create a sketch on the front plane. Once sketching

on the front plane, the convert geometry tool was used to convert the imported shape into a sketch which could be worked with. When the imported shape has been converted into sketch geometry, the profile of the shape could be closed using the line tool. The shape was then extruded a small amount to create the ice shape. Finally, the cross-section of the extruded ice shape was selected by left clicking on it and the section properties tool was selected. The section properties tool displayed all the cross-sectional area properties, including the second-moments of area which were required for the model to be run as well as the location of the centroid. The chord was measured by drawing two lines, one at the trailing edge of the ice shape and the other at the leading edge. The distance between was measured using the dimensions tool. A generated 3D model of an ice shape is shown in Figure 3.17.
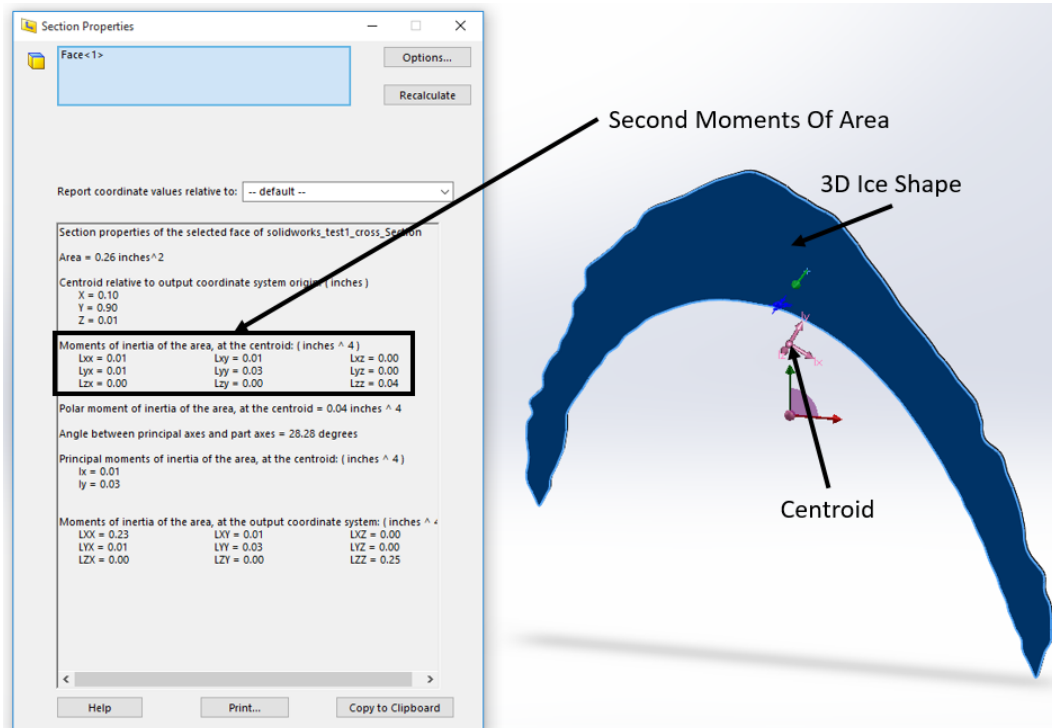
Figure 3.17. Example 3D Ice Shape Generated Using SolidWorks

65

3.3.3 Ultimate Tensile Strength Measurements

3.3.3.1 Beam Bending Test Rig

To validate the Euler-Bernoulli bending stress model presented in Chapter 2, the ultimate tensile strength of impact ice needed to be known. Since the values presented in literature vary widely, the ultimate tensile strength needed to be experimentally measured. A beam bending test rig was designed and built to perform this measurement. This section discusses the first and second generation designs.

3.3.3.1.1 First Generation Design The first generation beam bending rig consisted of two wooden stools with a thin walled piece of plastic placed on the top of each stool. The thin walls mimicked a pinned support configuration for each end of the ice beam. The containers were kept from moving by placing weights on top of them. The stools were then positioned such that the distance from the end of the plastic container on one stool to the container on the opposite stool was 22 inches. To fracture the ice beam, fishing line was tied around the mid-span and attached to a load plate of known weight. Weights were then added to the load plate in 20 gram increments until the ice fractured. A picture of the configuration and diagram of the model can be seen in Figure 3.18.

The first generation design has two drawbacks. First, by loading in 20 gram increments, the failure load is not precisely known. Second, the stools and thin walled pieces of plastic used are not an ideal way of creating a simply supported configuration. The first generation design did successfully provide ultimate strength values for the ice, but it was ultimately upgraded to improve the resolution of the data.
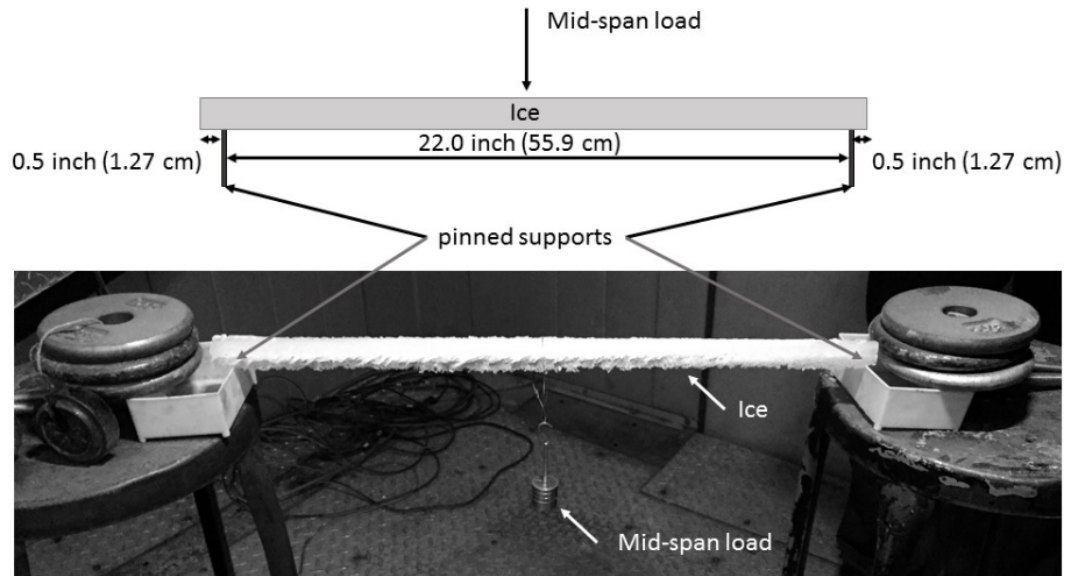
Figure 3.18. First Generation Beam Bending Rig with Simplified Schematic

3.3.3.1.2 Second Generation Design The second generation design aimed to improve on the two drawbacks of the first generation design. First, the stools and plastic containers were removed and replaced with a sturdier configuration. The base consisted of two steel angle iron brackets. Steel was selected so that the base would not move under loads applied to the ice beam. The steel brackets were fixed 22 inches apart by two aluminum beams which were horizontally bolted at the end of the bottom flanges. Four aluminum angle brackets were vertically bolted to the end of the upper flanges on the steel bracket (2 aluminum brackets to each steel bracket). Finally, an aluminum beam was bolted across the aluminum angle brackets on each steel bracket in order to create the simply supported configuration.

The second problem was solved by removing the load hanger and mass system and replacing it with a pneumatic system. A pneumatic lever arm was attached to a structure made out of steel channel. The structure allowed the lever arm to be suspended above the two simple supports holding the ice column and provide the transverse load needed to break the ice. Attached to the pneumatic lever arm was

an Interface fully sealed load cell with a 250 lb (1112 N) range. The load cell used can be seen in Figure 3.19.

Figure 3.19. 250 lb Range Interface Sealed Load Cell

Using a load cell allowed force to be measured over time as the breaking experiment was conducted. The force-time history provided by the load cell allowed the exact amount of force required to break the ice column to be determined, a schematic and picture of the second generation design can be seen in Figure 3.20.
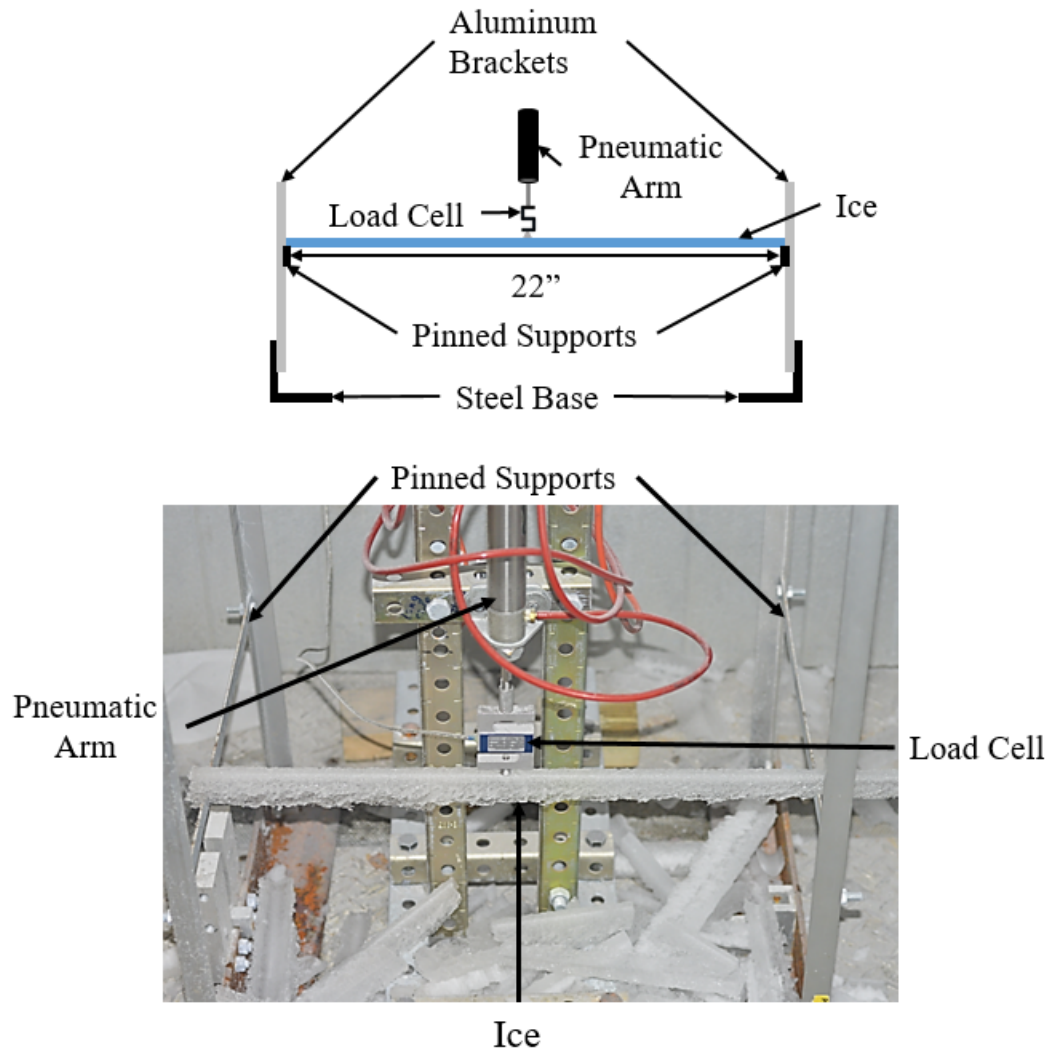
Figure 3.20. Second Generation Beam Bending Rig Structure

The data created by the load cell was collected using an in house LabVIEW code. This LabVIEW code was designed to collect force measurements over the duration of the test (force time history) and also contained a bias feature (for zeroing the recorded load prior to starting an experiment). A Porter Cable 135psi compressor was used to supply the needed air pressure to the pneumatic lever arm.

3.3.3.2   Procedure

After the ice shedding event was captured and the rotor was stopped, the remaining ice column on blade two could be tested using the second generation beam bending test rig. Removal of the ice column from the blade was accomplished using the de-icing system attached to the blade. The heaters on the blade were powered using a variable autotransformer (variac). Using a variac allowed the heat to be applied in a slow controlled manner until the ice delaminated from the blade surface. Starting from 0% power, the variac was slowly turned up to approximately 60%. Once at 60%, the ice beam was slowly, and with very little force, pulled off the blade surface. Note, pulling too quickly or too hard on the ice would result in the ice breaking into pieces too small to test.

Once removed from the blade, the ice beam was cut to a length of 23 in (58.4 cm) using a hot plate. This gave an effective beam length of 22 in (55.9 cm) with an overhang of 0.5 in (1.3 cm) on either side of the pinned boundaries. The 0.5 in of overhang at each end of the ice beam was leveled by touching it to a hot plate. The ice was then placed on the beam bending rig with the leading edge face up, reference Figure 3.20. Next, the load cell was biased to zero on the LabVIEW program and the load cell was then placed within contact of the ice beam. Data collection on LabVIEW was started and the regulator on the compressor was slowly opened until the ice fractured. LabVIEW saved the data as a text file which was then imported into excel for determination of the fracture load. As shown in Figure 3.21, the force increases to a peak and then decreases. The fracture load was taken to be the maximum value of this peak and based on the calibration of the load cell was in units of pounds. As described in detail in the "Ice Shape Cross-Sectional Properties" section, the fractured ice was set on a box, with the fracture face parallel with the

boxes edge. Underneath the box was a piece of grid paper for image calibration. The fracture cross-section was photographed using the same digital camera and flash described earlier in this chapter and the image processing was also done using the same process that was described in detail earlier. The photograph and image processing is necessary to determine the second moments of area as well as the centroid for calculation of the ultimate tensile stress. An example of a fracture cross-section photograph can be seen in Figure 3.22.
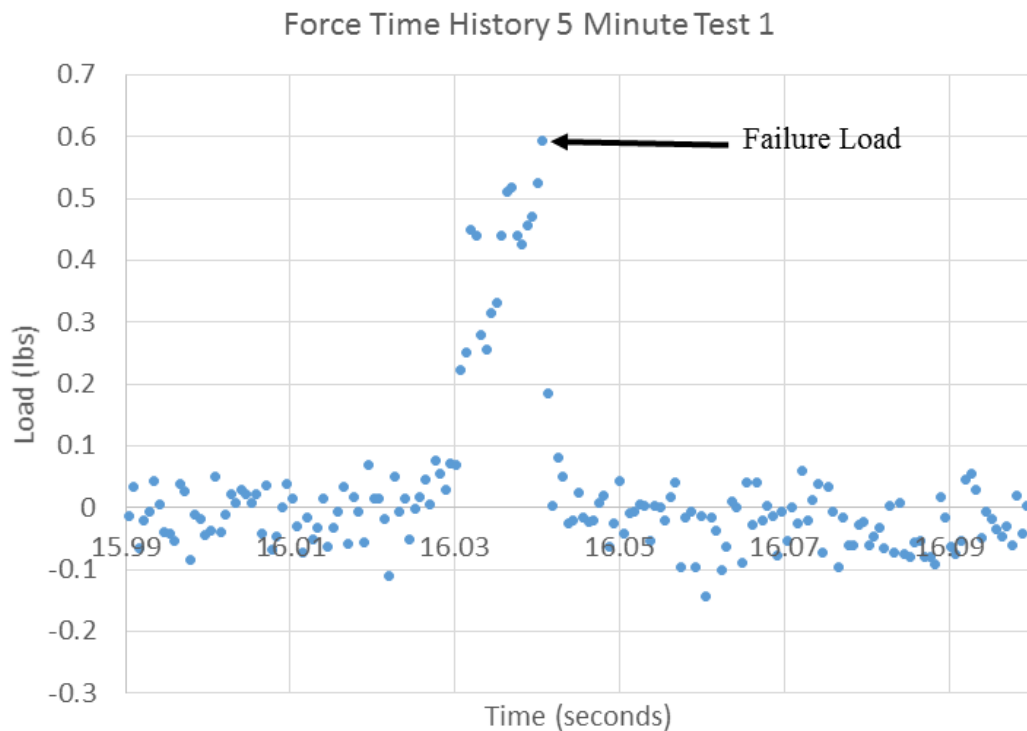
Figure 3.21. 5 Minute Test 1 Zoomed in Force Time History
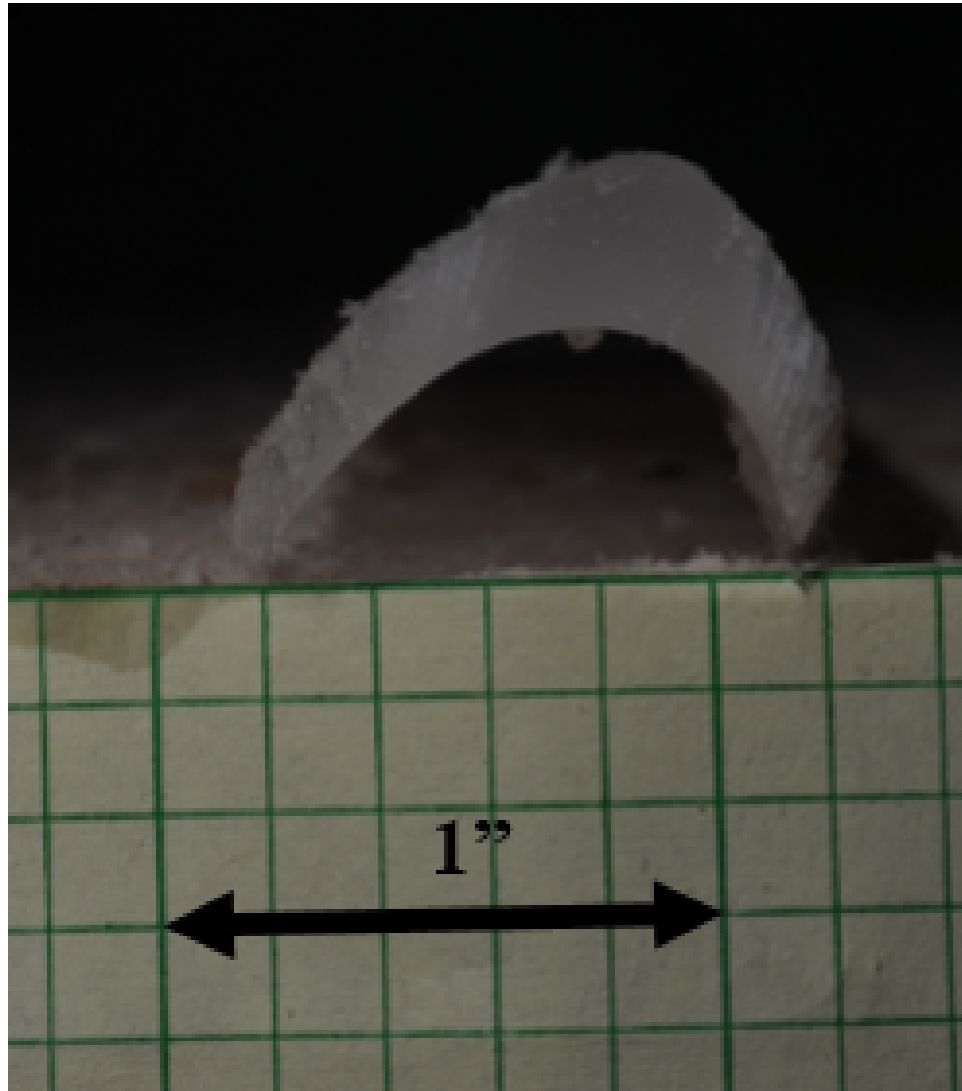
Figure 3.22. 5 Minute Test 1 Fracture Cross Section

As already discussed in Chapter 2, the maximum tensile stress is due to a bending moment created by a load. In the case of this experiment only a single point load was applied to the mid-span of the ice beam. Taking the boundary conditions into consideration (pinned at both ends), the bending moment can be found using Equation 3.1, where l is the mid-span distance of the ice beam (11in) and p is the point load determined from the load cell data. This bending moment

along with the cross-sectional area properties can be substituted into Equation 2.13 from Chapter 2 to determine the value of ultimate tensile stress.

$$M_x = \frac{pl}{4} \tag{3.1}$$

Chapter 4

Results and Model Validation

4.1 Experimental Results

This section presents and discusses data that was acquired experimentally. First, the experimental ultimate tensile strength is presented and discussed. Next, the experimental test data for three minutes of ice accretion is also presented and discussed. The discussion includes the calculation of the second moments of area of the ice shapes, the distances from the centroid to the point of maximum tensile stress, and the projectile lengths collected during the shedding experiment. Finally, the experimental data for five minutes of ice accretion is presented and discussed. The analysis includes the calculation of the second moments of area of the ice shapes, the distances from the centroid to the point of maximum tensile stress, and the projectile lengths collected during the shedding experiment with the high-speed cameras.

4.1.1 Ultimate Tensile Strength

Eight ultimate tensile strength (UTS) tests were performed on impact ice. The results of these tests can be seen in Figure 4.1. The mean of the data set was found to be 0.685 MPa with a standard deviation of ± 0.262 MPa. This standard deviation is equivalent to 38.4% of the mean and is similar to the standard deviations reported for the values of ultimate tensile strength presented in the literature and summarized in Chapter 1. In the Figure referenced above, a black bar represents the mean of the data set, and the gray box represents the standard deviation.

Experimental Ultimate Tensile Strength
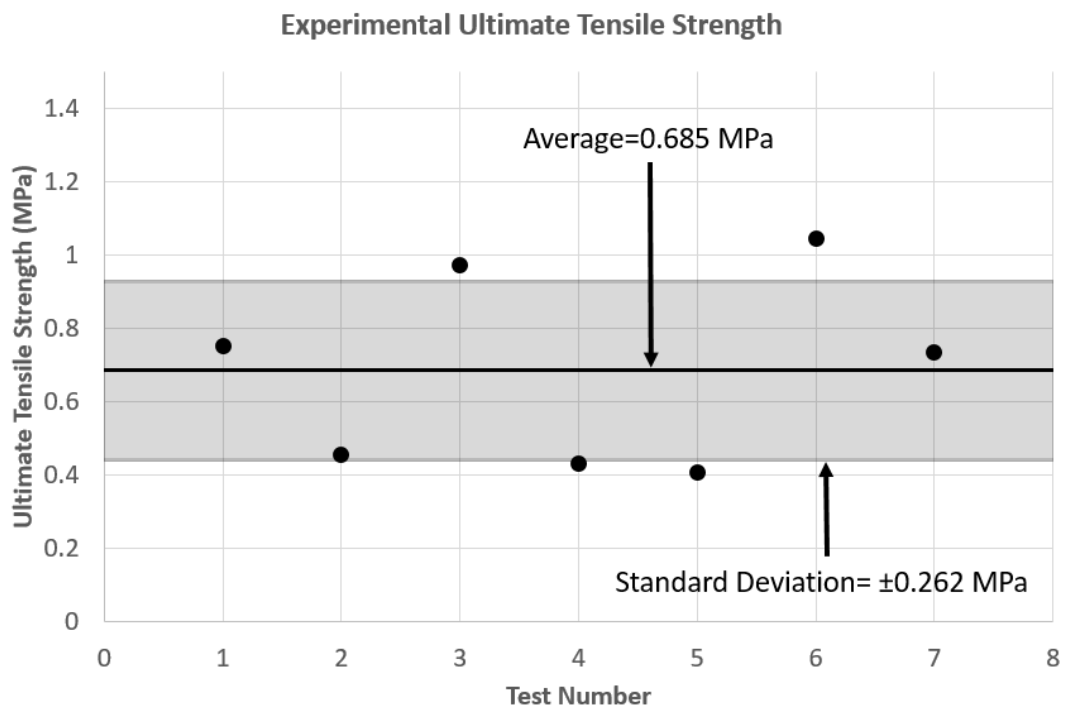
Figure 4.1. Graph of Experimental Ultimate Tensile Strength Data

4.1.2 Three Minute Experimental Test Data

4.1.2.1 Ice Cross-Section Experimental Data

At three minutes of ice accretion, eight experimental ice projectile lengths were acquired from six separate tests. Some of the tests had multiple cases (more then one projectile during the same shedding event). Each of those projectile lengths has corresponding experimental ice cross-section measurements that were acquired using the procedure described in Chapter 3. When there were multiple ice projectiles in a given shedding test, the ice beam on blade two was discretized and the cross-sectional area properties were approximated closer to the break face when possible. The measurements for the second moments of area, chords, and distances from the centroid to the point of maximum tensile stress are summarized in Table 4.1. Test 5 and 6, corresponding to case 4a and 4b, had cross-sectional area properties taken from a discretized ice beam. For the rest of the tests, the cross-sectional properties were taken of the ice shape at the tip of the shedding blade prior to turning the electro-thermal ice protection system on and inducing the ice to shed.

Table 4.1. Table of Experimental Second Moments of Area, Chords, and Distances to the Centroid Measurements for 3 Minute Tests

Test Number (Case)	Ixx (in^4)	Iyy (in^4)	Ixy (in^4)	$\bar{y}$ (in)	$\bar{x}$ (in)	chord (in)
1 (1a)	0.01833	0.03171	-0.00625	0.38393	0.04907	0.97874
2 (1b)	0.01833	0.03171	-0.00625	0.38393	0.04907	0.97874
3 (2a)	0.0439	0.06312	-0.02063	0.47965	0.07071	1.1339
4 (3a)	0.04813	0.08027	-0.02402	0.49219	0.12003	1.10461
5 (4a)	0.01213	0.02564	-0.00909	0.33437	0.10199	0.85636
6 (4b)	0.00296	0.00922	-0.00262	0.22164	0.07105	0.52846
7 (5a)	0.08123	0.08503	-0.03841	0.56502	0.12346	1.32654
8 (6a)	0.02443	0.0555	-0.00819	0.4016	0.0113	0.92476

4.1.2.2 Ice Projectile Length Measurements

As stated in the section above, there were eight ice projectile length measurements acquired at three minutes of ice accretion. These length measurements are summarized in Table 4.2. The average length of the ice projectiles for three minutes of ice accretion was found to be 4.5 inches. The data set has a standard deviation of ±0.916 inches, which is 20.4% of the mean value. The average length of the first shed projectiles is 4.93 inches with a standard deviation of ±0.689 inches (14% of the mean value). Tests 1 and 2, corresponding to case 1a and 1b, have projectile lengths of 4.421 and 4.370 inches, respectively. The projectile length decreases by 1.2% from the first to the second projectile. Tests 5 and 6, corresponding to case 4a and 4b, have projectile lengths of 3.773 and 3.250 inches. The projectile length decreases by 13.8% from the first to the second projectile. It was assumed that the

amount of ice accreted would linearly decrease as the span-wise location changes from the tip to the root, resulting in the ice projectiles becoming smaller as each subsequent projectile is shed from the blade and the results from tests 1, 2, 5, and 6 show this trend.

Table 4.2. Ice Projectile Length Results from Three Minute Ice Accretion Shedding Tests

Test Number (Case)	Ice Projectile Length (inches)
1 (1a)	4.421
2 (1b)	4.370
3 (2a)	4.626
4 (3a)	6.366
5 (4a)	3.773
6 (4b)	3.250
7 (5a)	4.271
8 (6a)	4.960
Average	**4.50**
Standard Deviation	**0.916**

4.1.3 Five Minute Experimental Test Data

4.1.3.1   Ice Cross-Section Experimental Data

At five minutes of ice accretion, ten experimental ice projectile lengths were acquired from five separate tests. Some of the tests had multiple cases (more then one projectile during the same shedding event). Each of those projectile

lengths has corresponding experimental ice cross-section measurements that were acquired using the procedure described in Chapter 3. When there were multiple ice projectiles in a given shedding test, the ice beam on blade two was discretized and the cross-sectional area properties were approximated closer to the break face when possible. The measurements for the second moments of area, chords, and distances from the centroid to the point of maximum tensile stress are summarized in Table 4.3. Tests 1, 2, 3, 6, 7, 9 and 10, corresponding to cases 1a, 1b, 1c, 3a, 3b, 5a and 5b respectively, had cross-sectional area properties taken from discretized ice beams. For the rest of the tests, the cross-sectional area properties were taken of the ice shape at the tip of the shedding blade prior to turning the electro-thermal ice protection system on and inducing the ice to shed.

Table 4.3. Table of Experimental Second Moments of Area, Chords, and Distances to the Centroid Measurements for 5 Minute Tests

Test Number (Case)	Ixx (in^4)	Iyy (in^4)	Ixy (in^4)	$\bar{y}$ (in)	$\bar{x}$ (in)	chord (in)
1 (1a)	0.02948	0.04724	-0.01324	0.43792	0.06867	1.08041
2 1(b)	0.00649	0.01626	-0.00433	0.3045	0.06979	0.67118
3 1(c)	0.00629	0.01613	-0.00437	0.29664	0.05963	0.69454
4 (2a)	0.03065	0.04566	-0.01513	0.44108	0.05414	1.01337
5 (2b)	0.03065	0.04566	-0.01513	0.44108	0.05414	1.01337
6 (3a)	0.02533	0.05082	-0.00829	0.42525	0.05612	0.98591
7 (3b)	0.0061	0.01682	-0.00451	0.29397	0.06138	0.63256
8 (4a)	0.02752	0.05512	-0.01033	0.43049	0.04421	0.98044
9 (5a)	0.0591	0.08909	-0.03363	0.51266	0.10982	1.09102
10 (5b)	0.06929	0.08295	-0.04481	0.55509	0.162	1.17229

4.1.3.2   Ice Projectile Length Measurements

As stated in the section above, there were ten ice projectile length measurements acquired at five minutes of ice accretion. These length measurements are summarized in Table 4.4. The average length of the ice projectiles for five minutes of ice accretion was found to be 5.20 inches. The data set has a standard deviation of ± 1.13 inches, which is 21.7% of the mean value. The average length for the first shed projectiles is 6 inches with a standard deviation of ± 0.567 inches (9.45% of the mean). The length for five minutes of accretion for the first shed ice projectile is 19.6% higher than for the three minute tests. Since five minutes of ice accretion should result in thicker ice, it should also result in longer ice projectiles. The average length for the second shed projectiles is 4.62 inches with a standard deviation of ± 0.933 inches (20.2% of the mean). The decrease in measured projectile lengths between the first and second projectiles is consistent with the assumption of a linear decrease in accreted ice on the leading edge as the radial distance between the blade tip and rotor decreases.

Table 4.4. Ice Projectile Length Results from Five Minute Ice Accretion Shedding Tests

Test Number (Case)	Ice Projectile Length (inches)
1 (1a)	5.115
2 (1b)	3.905
3 (1c)	3.542
4 (2a)	6.233
5 (2b)	4.680
6 (3a)	6.700
7 (3b)	3.979
8 (4a)	5.590
9 (5a)	6.334
10 (5b)	5.919
Average	**5.20**
Standard Deviation	**1.13**

4.2 Model Prediction Improvements

In chapter 2, the model was originally developed assuming the ice shapes would have symmetric cross-sections. While performing testing and initial data processing it was noticed that the ice shapes were not symmetrical about either the x or y axis. This led to the bending stress equation being re-derived into its most general form to account for the lack of symmetry. The critical ice lengths were predicted using both assumptions for comparison.

4.2.1 Three Minute Tests

Assuming symmetric ice shapes, Equation 2.4 is used to calculate the bending moment, M, where σ is equal to the UTS reported in the above section, c is equal to $\bar{y}$ from the "Three Minute Experimental Test Data" section, and I is equal to Ixx also from "Three Minute Experimental Test Data" section. Finally, Equation 2.3 is used solve for the critical projectile length, l. Assuming a non-symmetric ice shape, Equation 2.13 is used to solve for the bending moment, M, using the cross-sectional properties reported in the "Three Minute Experimental Test Data" section and the UTS reported at the start of the Chapter. Finally, Equation 2.3 is used to solve for the critical projectile length, l. The model predictions for the three minute test cases using both sets of assumptions are summarized in Table 4.5. As can be seen, the projectile length prediction decreases when taking into account the fact that the cross-sections are not symmetric.

Table 4.5. Ice Projectile Length Model Predictions Using Three Minute Ice Shape Data

Test Number (Case)	Symmetric Ice Shape Assumption	Non-Symmetric Ice Shape Assumption
1 (1a)	4.856	4.632
2 (1b)	4.856	4.632
3 (2a)	6.246	5.613
4 (3a)	6.542	5.825
5 (4a)	4.525	3.684
6 (4b)	3.495	2.895
7 (5a)	7.238	6.123
8 (6a)	5.639	5.486

4.2.2 Five Minute Tests

Assuming symmetric ice shapes, Equation 2.4 is used to calculate the bending moment, M, where σ is equal to the UTS reported at the start of this chapter, c is equal to $\bar{y}$ from the "Five Minute Experimental Test Data" section, and I is equal to Ixx also from "Five Minute Experimental Test Data" section. Finally, Equation 2.3 is used solve for the critical projectile length, l. Assuming a non-symmetric ice shape, Equation 2.13 is used to solve for the bending moment, M, using the cross-sectional properties reported in the "Five Minute Experimental Test Data" section and the UTS reported at the start of the chapter. Finally, Equation 2.3 is used to solve for the critical projectile length, l. The model predictions for the five minute test cases using both sets of assumptions are summarized in Table 4.6. As was seen in the model predictions for the three minute test cases, the length predictions decrease when assuming a non-symmetric ice shape. When looking at tests 1, 2, 3, 6, 7, 9 and 10 (the tests that have cross-sectional area properties from a discretized ice beam) it can be seen that the predicted projectile length decreases after each subsequent projectile. The decrease observed here further validates the assumption of a linear decrease in accreted ice on the leading edge as the radial distance between the tip and rotor decreases.

Table 4.6. Ice Projectile Length Model Predictions Using Five Minute Ice Shape Data

Test Number (Case)	Symmetric Ice Shape Assumption	Non-Symmetric Ice Shape Assumption
1 (1a)	5.488	5.022
2 (1b)	3.918	3.449
3 (1c)	3.842	3.371
4 (2a)	5.757	5.162
5 (2b)	5.757	5.162
6 (3a)	5.404	5.202
7 (3b)	3.982	3.470
8 (4a)	5.614	5.362
9 (5a)	7.147	6.091
10 (5b)	7.174	5.379

4.3 Model Prediction and Experimental Projectile Lengths Comparison

4.3.1 Symmetric Ice Shape Assumption

4.3.1.1 Three Minute Tests

The experimentally measured ice projectile lengths for the three minute ice accretion tests were compared to the model predictions assuming a symmetrical ice shape. A bar graph showing a test by test comparison of the experimental measurement versus the model prediction can be seen in Figure 4.2. A percent difference was calculated between the model prediction and the experimental

measurement for each test. The average percent difference was found to be 17.77%
These results are summarized in Table 4.7. The tests with projectile length
predictions calculated using cross-sectional area properties from a discretized ice
beam (Test 5 (4a) and 6 (4b)) have a percent difference between experimental
measurement and model prediction of 12.71%, which is 42% lower than the percent
difference for the rest of the three minute test cases (19.47%).

Model Prediction Assuming Symmetric Cross Section Compared to 3 Minute Experimental Tests

Figure 4.2. Graph Comparing Model Predicted Projectile Lengths Assuming Symmetric
Ice Shapes to Experimental Data for the 3 Minute Tests

Table 4.7. Data Table Comparing Model Predictions for a Symmetric Ice Shape Assumption to 3 Minute Experimental Projectile Lengths

Test Number (Case)	Model Prediction (inches)	Experimental Measurement (inches)	Percent Difference
1 (1a)	4.86	4.42	9.37%
2 (1b)	4.86	4.37	10.53%
3 (2a)	6.25	4.63	29.81%
4 (3a)	6.54	6.37	2.72%
5 (4a)	4.53	3.77	18.14%
6 (4b)	3.50	3.25	7.27%
7 (5a)	7.24	4.27	51.55%
8 (6a)	5.64	4.96	12.81%
Average			**17.77%**

4.3.1.2 Five Minute Tests

The experimentally measured ice projectile lengths for the five minute ice accretion tests were compared to the model predictions assuming a symmetrical ice shape. A bar graph showing a test by test comparison of the experimental measurement versus the model prediction can be seen in Figure 4.3. A percent difference was calculated between the model prediction and the experimental measurement for each test. The average percent difference was found to be 9.72% These results are summarized in Table 4.8. The percent difference between the model and the experimental lengths for the 5 minute cases is 58% lower than for the 3 minute cases. This is likely due to the increased thickness of the ice mitigating some of the measurement uncertainty when determining the second moments of area

and distances from the centroid to the point of maximum tensile stress. Averaging the percent differences of both the 3 and 5 minute cases yields a percent difference of 13.3% under the assumption of symmetric ice shapes. The tests with projectile length predictions calculated using cross-sectional area properties from a discretized ice beam (Test 1 (1a), 2 (1b), 3(1c), 6 (3a), 7 (3b), 9 (5a), and 10 (5b)) have a percent difference between experimental measurement and model prediction of 9.7%, which is the same as the percent difference for the rest of the five minute test cases (9.7%).
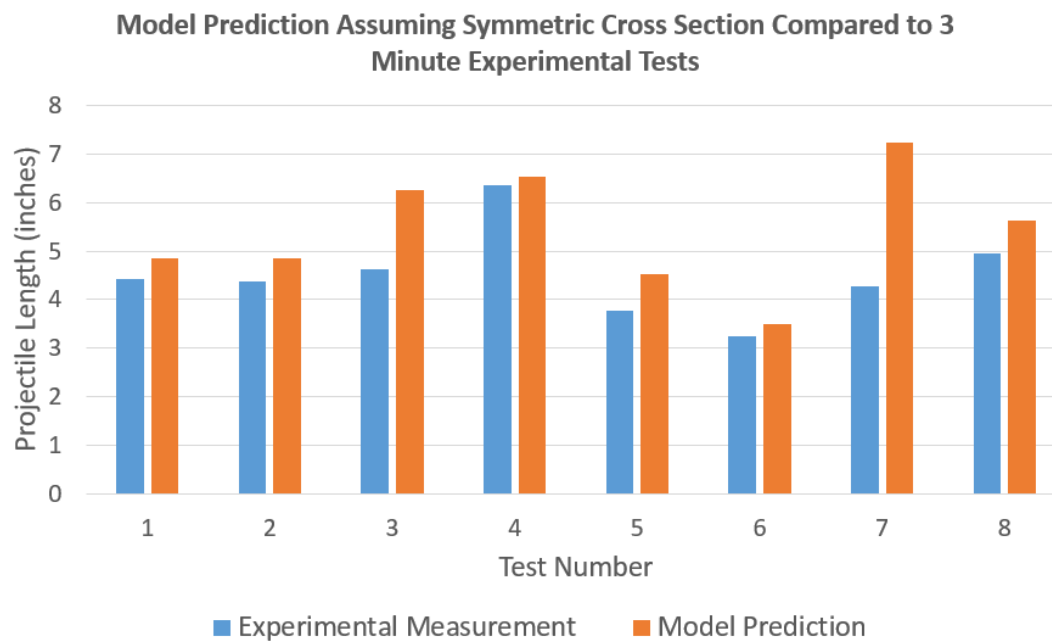

Figure 4.3. Graph Comparing Model Predicted Projectile Lengths Assuming Symmetric Ice Shapes to Experimental Data for the 5 Minute Tests

87

Table 4.8. Data Table Comparing Model Predictions for a Symmetric Ice Shape Assumption to 5 Minute Experimental Projectile Lengths

Test Number (Case)	Model Prediction (inches)	Experimental Measurement (inches)	Percent Difference
1 (1a)	5.49	5.1149	7.04%
2 (1b)	3.92	3.91	0.33%
3 (1c)	3.84	3.54	8.10%
4 (2a)	5.76	6.23	7.93%
5 (2b)	5.76	4.68	20.65%
6 (3a)	5.40	6.70	21.41%
7 (3b)	3.98	3.978	0.09%
8 (4a)	5.61	5.59	0.43%
9 (5a)	7.15	6.33	12.07%
10 (5b)	7.17	5.92	19.17%
Average			**9.72%**

4.3.2 Non-Symmetric Ice Shape Assumption

4.3.2.1 Three Minute Tests

The experimentally measured ice projectile lengths for the three minute ice accretion tests were also compared to the model predictions assuming a non-symmetric ice shape. A bar graph showing a test by test comparison of the experimental measurement versus the model prediction can be seen in Figure 4.4. A percent difference was calculated between the model prediction and the experimental measurement for each test. The average percent difference was found to be 12.29%

These results are summarized in Table 4.9. The percent difference between the model and the experimental lengths for three minutes assuming non-symmetric ice shapes is 36.5% lower than the assumption of symmetric ice shapes. Using the assumption of non-symmetric ice shapes, the tests with projectile length predictions calculated using cross-sectional area properties from a discretized ice beam (Test 5 (4a) and 6 (4b)) have a percent difference between experimental measurement and model prediction of 6.97%, which is 67.4% lower than the percent difference for the rest of the three minute test cases (14.06%).
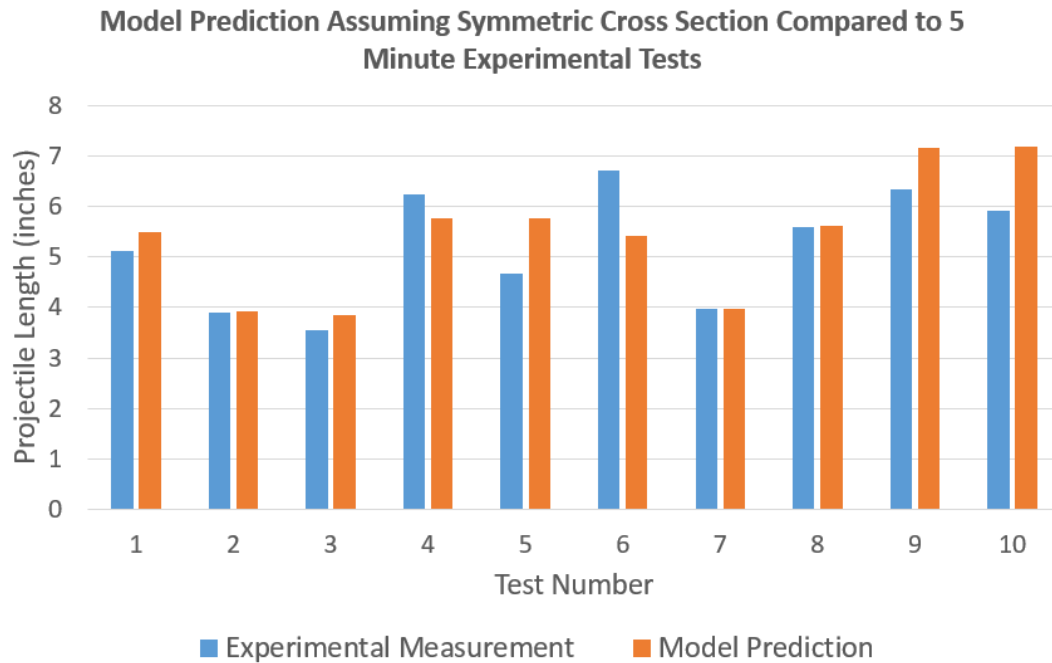

Figure 4.4. Graph Comparing Model Predicted Projectile Lengths Assuming Non-Symmetric Ice Shapes to Experimental Data for the 3 Minute Tests

Table 4.9. Data Table Comparing Model Predictions for a Non-symmetric Ice Shape Assumption to 3 Minute Experimental Projectile Lengths

Test Number (Case)	Model Prediction (inches)	Experimental Measurement (inches)	Percent Difference
1 (1a)	4.63	4.42	4.65%
2 (1b)	4.63	4.37	5.82%
3 (2a)	5.61	4.63	19.28%
4 (3a)	5.82	6.37	8.88%
5 (4a)	3.68	3.77	2.38%
6 (4b)	2.89	3.25	11.56%
7 (5a)	6.12	4.27	35.63%
8 (6a)	5.49	4.96	10.08%
Average			**12.29%**

4.3.2.2   Five Minute Tests

The experimentally measured ice projectile lengths for the five minute ice accretion tests were also compared to the model predictions assuming a non-symmetric ice shape. A bar graph showing a test by test comparison of the experimental measurement versus the model prediction can be seen in Figure 4.5. A percent difference was calculated between the model prediction and the experimental measurement for each test. The average percent difference was found to be 10.43% These results are summarized in Table 4.8. This percent difference is 16.4% lower than for the 3 minute cases. Again, this is likely due to the increased thickness of the ice mitigating some of the uncertainty in the measurements for the second moments of area and distances from the centroid to the point of maximum

tensile stress.

The percent difference of 10.43% between the model and the experimental lengths for five minutes assuming non-symmetric ice shapes is actually 7% higher than the assumption of symmetric ice shapes. While this is unexpected, the average percent difference of both the 3 and 5 minute cases, assuming non-symmetric cross-sections, yields an average percent difference of 11.3%, which is 16.3% lower than the assumption of symmetric cross-sections (13.3%). Using non-symmetric ice shape assumptions, the tests with projectile length predictions calculated using cross-sectional area properties from a discretized ice beam (Test 1 (1a), 2 (1b), 3(1c), 6 (3a), 7 (3b), 9 (5a), and 10 (5b)) have a percent difference between experimental measurement and model prediction of 10.21%, which is 6.7% lower than the percent difference for the rest of the five minute test cases (10.92%). Overall, the model predictions which had cross-sectional area properties more representative of the break face of each ice projectile were on average 37% closer to the corresponding experimental length measurements.
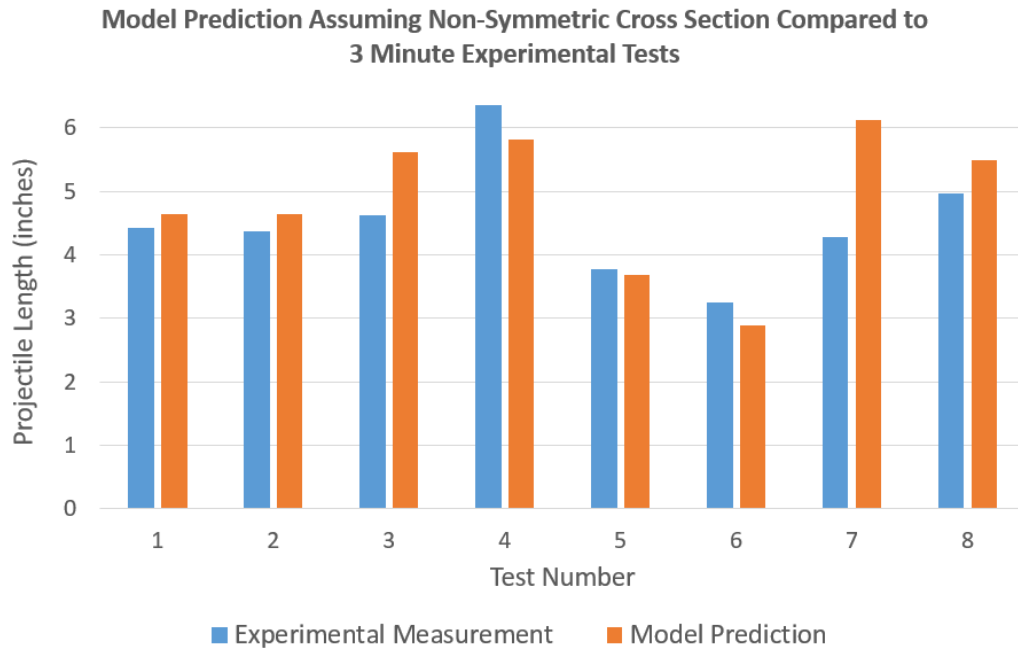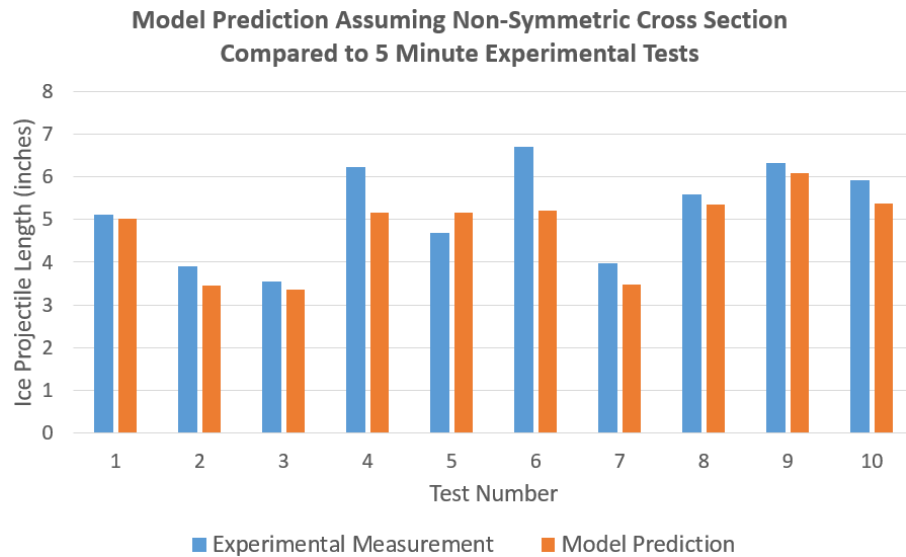

Figure 4.5. Graph Comparing Model Predicted Projectile Lengths Assuming Non-Symmetric Ice Shapes to Experimental Data for the 5 Minute Tests

Table 4.10. Data Table Comparing Model Predictions for a Non-Symmetric Ice Shape
Assumption to 5 Minute Experimental Projectile Lengths

Test Number (Case)	Model Prediction (inches)	Experimental Measurement (inches)	Percent Difference
1 (1a)	5.02	5.11	1.83%
2 (1b)	3.45	3.91	12.40%
3 (1c)	3.37	3.54	4.97%
4 (2a)	5.16	6.23	18.80%
5 (2b)	5.16	4.68	9.79%
6 (3a)	5.20	6.70	25.17%
7 (3b)	3.47	3.98	13.66%
8 (4a)	5.36	5.59	4.17%
9 (5a)	6.09	6.33	3.90%
10 (5b)	5.38	5.92	9.57%
Average			**10.43%**

Chapter 5

Conclusions and Recommendations for Future Work

5.1 Conclusions

The goal of this thesis was to develop a tool for predicting the projectile length of shed ice from a rotating blade under representative in-flight icing conditions and due to the effects of natural shedding induced by centrifugal forces and/or assisted by electro-thermal ice protection systems. In this chapter the main conclusions obtained during the work are summarized.

5.1.1 Modeling Tool

Two mathematical models were investigated when developing the prediction tool, an Euler-Bernoulli model based on direct tensile stress failure and a Timoshenko model based on direct transverse shear failure. Equations for both models were derived and presented in Chapter 2 and the models were compared against one another. The Euler-Bernoulli beam bending model based on direct tensile stress

failure was selected for developing the prediction tool, since the assumptions of the model were shown to be applicable for the size of the ice projectiles investigated, coupled with the fact that the Timoshenko model required additional assumptions. These additional assumptions added too much uncertainty into the model.

5.1.2 Experimental Configuration

To implement the prediction tool, a secondary goal of the thesis was to experimentally determine the corresponding ultimate strength of the failure mode. Since an Euler-Bernoulli beam bending model based on direct tensile stress failure was the accepted model, the corresponding ultimate strength which needed to be measured was the tensile strength of impact ice. The ultimate strength of the ice was acquired using in-flight representative impact ice accreted at the same icing conditions used for projectile measurements. The accreted ice was removed from the rotor and the ice beams were tested under pinned-pinned boundary conditions. A load was applied at the center of the beam until failure using a pneumatic lever arm and the force time history of each break experiment was collected using a load cell. The results of the tests yielded an ultimate tensile strength of 0.685 MPa, with a standard deviation of 38.4%. The standard deviation seen in this experiment was similar to the standard deviations seen in the results of similar tests presented in literature.

The model also required experimental second moments of area, distances from the centroid to the point of maximum tensile stress, and chord measurements. These were obtained from photographs of the ice shape at the tip of the shedding blade as well as from discretized ice beams. While the photographs of the ice shapes appear to create relatively similar shapes (as quantified at the tip of the

rotor), the experimental values for the second area moments of intertia extracted from each photograph varied due to variations on the ice accretion extension limits. These variations in second area moments of inertia resulted in different projectile lengths being predicted. Futhermore, the variation of ice thickness along the rotor blade (given the variation of ice accretion velocity) also provided a decreasing ice projectile length as the ice thickness decreased from tip to root.

When possible, the ice beam on blade two was removed and discretized into 4 inch segments to quantify the change in second area moments of inertia as the radial length between the blade tip and the rotor decreased. Discretization of the ice beam allows the second area moments of inertia closest to the break face of the ice projectile to be used in the proposed tool. When discretization of the ice beam was not possible, the second area moments of inertia were calculated using the ice shape on the tip of the shedding blade, prior to inducing shedding. High-speed cameras were used to acquire images of the ice projectiles during the shedding events, allowing the experimental lengths to be quantified. Experimental data was acquired for ice accreted at three minutes and at five minutes, resulting in data sets for two different ice thicknesses. The average ice projectile length of the three minute experiments was found to be 4.5 inches and the length of the five minute experiments was found to be 5.2 inches. The ice projectiles created in the five minute tests were expected to be longer in length due to the ice being thicker and requiring a larger force to break. In a given test, the first ice projectiles shed from the rotor blade was expected to be longer than subsequent ice projectiles shed during the same test due to the ice being thicker at the tip of the blade.The standard deviations in the lengths of the ice projectiles (3 minutes and 5 minutes of ice accretion) was 20.4% and 21.7%. The uncertainty in this data set is attributed to taking into account all data points in both sets, regardless of whether it was a first

or second shed projectile. When looking at just the first ice projectile during each shedding test, the standard deviation of the experimentally determined projectile lengths for the 3 and 5 minute tests resepectively are 17.12% and 10.55%. The standard deviation for the second ice projectile during each shedding test for the 3 and 5 minute tests respectively are 10.37% and 10.21%.

5.1.3 Prediction Tool Validation

The final step to achieving the goal of the research was to compare the experimentally obtained ice projectile lengths to the lengths predicted by the model. In addition, the model was developed assuming both symmetric and non-symmetric ice shape cross-sections, and predicted results for both scenarios were also compared. The percent difference between the model predictions and the experimental three minute test data was found to be 17.77% using a symmetric cross-section assumption, and 12.29% assuming a non-symmetric cross-section. The percent difference between the model predictions and the experimental five minute tests was found to be 9.72% using a symmetric cross-section assumption, and 10.43% assuming a non-symmetric cross-section. These results include multiple fracturing events for a given shed test. The average percent difference for both accretion times assuming symmetric ice shapes was found to be 13.3%, compared to 11.3% when assuming non-symmetric ice shapes. For the test cases where projectile lengths were predicted using cross-sectional area properties obtained from a discretized ice beam, the average percent difference between the model prediction and experimental length was found to be 8.6%, compared to 13% for the predictions using cross-sectional properties which were estimated using the ice shape at the tip of the rotor blade. The main conclusion from these comparisons is that the cross-sectional

properties of the ice projectiles fracture face need to be known in order for the model to correctly predict the projectile length.

5.2 Recommendations for Future Work

5.2.1 Model Improvements

5.2.1.1 Drag Coefficient

One of the main assumptions made in developing the prediction tool was in regards to the coefficient of drag. The ice shapes were assumed to be "C" shapes and as such, the known value from literature of 1.2 was used. This assumption may not be entirely accurate, as this assumes a smooth C shape. The ice shapes themselves however, are not smooth. A computational fluid dynamics program such as ANSYS could be used to determine a more accurate value for the drag coefficient at given test conditions. The coefficient could also be determined through experimental testing where molds are created from the ice shapes and then tested in a wind tunnel to capture drag coefficients.

5.2.1.2 Timoshenko Model

The main reason a Timoshenko model was not used for the prediction tool in this thesis is due to the fact that additional assumptions about the shear correction factor and the ultimate shear strength of impact ice needed to be made. The ultimate shear strength used in the model comparison in Chapter 2 was found using Von Mises Stress Criterion. This approach works well for metals such as aluminum, however ice is not a metal and the ultimate shear stress of the impact ice might be significantly lower than the stress predicted using this criterion. Experimental

determination of the ultimate shear stress would eliminate this source of uncertainty. In addition, a numerical approach to finding the shear correction factor would further eliminate that source of uncertainty. With both of these two values, a Timoshenko approach could be revisited and properly analyzed.

5.2.1.3 LEWICE

LEWICE is an ice shape prediction code developed by NASA. It was explored as an option to eliminate the need of having to find experimental second moments of area, distances from the centroid to the point of maximum tensile stress, and chord measurements. This would truly allow the model developed in this thesis to become a prediction tool. Initial results from LEWICE revealed that the code is failing to predict ice feather build and connection to the main ice shape. This results in a significantly smaller ice projectile length predictions than what is actually experimentally measured, since the effective cross-sectional area of the fracturing beam is smaller. Due to time constraints, a solution to this problem was not explored. Future work would involve investigating the collection efficiencies in the LEWICE code as well as other parameters to see if it is possible to correct the code to account for the build up and connection to the main shape of feathers accreted in the aft location.

5.2.1.4 Parameter Variation

Icing parameters including LWC, MVD and temperature were all held constant in this thesis. It is known that variations in these parameters cause not only variations in how the ice forms, but also in the physical properties. Future work could be done to document the effect of how variations in LWC, MVD and temperature affect the projectile lengths and ultimate tensile strength.

In addition, the airfoil used was symmetric and the angle of attack it was tested at was approximately 0°. Therefore, drag was the only significant force acting on the ice formation and so it was the only force considered in the analysis. In the future, changing the collective pitch and accounting for other aerodynamic forces would increase the capabilities of the model.

5.2.2 Blade Geometry

The final recommendation for future work involves alteration of the blade geometry at the tip. Can the tip of the blade be modified in such a way that the aerodynamic performance of the blade is not lost, while at the same time controlling the length of ice projectiles? Dr. Palacios currently has a patent on such a technology and further investigation is necessary.

Appendix A

Euler-Bernoulli Symmetric Ice Cross-Section Projectile Length Matlab Prediction Code

```
%intialize
    clc;
    clear;
    close;
%Constants
    IM=0.0254; %conversion constant for inches to meters, 0.0254 meters per inch
    E=9.5e9; %youngs modulus of impact ice (pascals)
    UTS=0.685e6; %ultimate tensile strength of impact ice, found experimentally
(pascals)
    r=1.651; %radius of blade (meters)
    Cd=1.2; %drag coefficient of C shape
    rho=1.29; %density of air (kg/m^3)
    rpm=350; %rotor speed in RPM
```

```
l=0:0.0000001:1; %length of ice (meters)
%Cross-Sectional Properties from SolidWorks
con=[0.01078 0.29055 1.09748]; %input 3 constants in this order - I ybar chord
I=con(1)*IM^4; %2nd moment of area about x axis - obtained from solidworks
(m^4)
c=con(2)*IM; %y distance from centroid to force
chord=con(3)*IM; %distance from front of ice shape to back of ice shape
%calculations
omega=rpm*2*pi/60; %rotor speed in Rad/s
v=omega*r %airflow velocity (m/s)
drag=0.5*rho*v^2*Cd*chord %drag of the ice shape
    for i=1:10000001
        moment=drag*((l(i))^2)/2; %resultant internal moment about neutral
axis (due to a constant distributed load)
        maxStress=moment*c/I; %maximum stress due to bending
            if maxStress>=UTS
                failureLength=l(i)/IM; %output ice size
                break
            end
    end
failureLength %output ice projectile length
```

Appendix B

Euler-Bernoulli Axisymmetric Ice Cross-Section Projectile Length Matlab Prediction Code

```
%intialize
    clc;
    clear;
%Constants
    IM=0.0254; %conversion constant for inches to meters, 0.0254 meters per inch
    E=9.5e9; %youngs modulus of impact ice (pascals)
    UTS=0.685e6; %ultimate tensile strength of impact ice, found experimentally
(pascals)
    r=1.651; %radius of blade (meters)
    Cd=1.2; %drag coefficient
    rho=1.29; %density of air (kg/m^3)
    rpm=350; %rotor speed in RPM
    l=0:0.0000001:1; %length of ice (meters)
```

/noindent %Cross-Sectional Properties from SolidWorks

con=[0.01078 0.01772 0.00254 0.29055 -0.06544 1.09748]; %input 6 constants in this order - Ixx Iyy Ixy ybar xbar chord

Ixx=con(1)*IM^4; %2nd moment of area about x axis - obtained from solidworks (m^4)

Iyy=con(2)*IM^4; %2nd moment of area about x axis - obtained from solidworks (m^4)

Ixy=con(3)*IM^4;%2nd moment of area about x axis - obtained from solidworks (m^4)

ybar=con(4)*IM; %y distance from centroid to force

xbar=con(5)*IM; %x distance from centroid to force

chord=con(6)*IM; %distance from front of ice shape to back of ice shape

%calculations

omega=rpm*2*pi/60; %rotor speed in Rad/s

v=omega*r %airflow velocity (m/s)

drag=0.5*rho*v^2*Cd*chord %drag of the ice shape

    for i=1:10000001

        Mx=drag*((l(i))^2)/2; %resultant internal moment about neutral axis (due to a constant distributed load)

        maxStress=(Mx*Iyy*ybar/(Ixx*Iyy-Ixy^2))-(Mx*Ixy*xbar/(Ixx*Iyy-Ixy^2)); %maximum stress due to bending of a non symmetric cross section

          if maxStress>=UTS

            failureLength=l(i)/IM; %output ice projectile length

            break

          end

    end

failureLength %output projectile length

Appendix C

Timoshenko FSDT Ice Length Shedding Prediction Code

%intialize

    clc;

    clear;

    close;

%Constants

    IM=0.0254; %conversion constant for inches to meters, 0.0254 meters per inch;

    E=9.5e9; %youngs modulus of impact ice (pascals)

    USS=0.3425e6; %ultimate shear strength of impact ice, found experimentally

(pascals)

    r=1.651; %radius of blade (meters)

    Cd=1.2; %drag coefficient

    rho=1.29; %density of air (kg/m^3)

    rpm=350; %rotor speed in RPM

    l=0:0.0000001:1; %length of ice (meters)

    k=0.1;

```
con=[0.54153 1.32654]; %input 2 constants in this order - cross-sectional area
and chord

    A=con(1)*IM^2;

    chord=con(2)*IM;
%calculations

    omega=rpm*2*pi/60; %rotor speed in Rad/s

    v=omega*r; %airflow velocity (m/s)

    drag=0.5*rho*v^2*Cd*chord %drag of the ice shape

        for i=1:10000001 %moment=drag*((l(i))^2)/2; %resultant internal moment
about neutral axis (due to a constant distributed load)

            maxStress=(drag*k/A)*(l(i)); %maximum stress due to bending

                if maxStress>=USS

                    failureLength=l(i)/IM; %output ice size

                    break

                end

            end

failureLength
```

Bibliography

[1] Federal Aviation Regulation "Part 25 Airworthiness Standards: Transport Category Airplanes and Part 29 Airworthiness Standards: Transport Category Rotorcraft," *FAA, Washington DC*.

[2] Soltis, J. T. *Design and Testing of an Erosion Resistant Ultrasonic De-Icing System for Rotorcraft Blades*, M.s. thesis, The Pennsylvania State University.

[3] Soltis, J., J. Palacios, T. Eden, and D. Wolfe (2015) "Evaluation of Ice Adhesion Strength on Erosion Resistant Materials," *AIAA Journal*, **Vol. 53**(No. 7), pp. 1825–1835.

[4] Han, Y. and J. Palacios (2012) "Analytical and Experimental Determination of Airfoil Performance Degradation Due to Ice Accretion," in *4th AIAA Atmospheric and Space Environments Conference*, New Orleans, Louisiana, pp. 1–25.

[5] Coffman, H. J. (1987) "Helicopter Rotor Icing Protection Methods," *Journal of the American Helicopter Society*, **32**.

[6] Overmeyer, A. D. (2012) *Actuator Bondline Optimization and Experimental Deicing of a Rotor Blade Ultrasonic Deicing System*, M.s. thesis, The Pennsylvania State University.

[7] Wright, J. and R. Aubert (2014) "Icing Wind Tunnel Test of a Full Scale Heated Tail Rotor," in *American Helicopter Society 70h Annual Forum*, 70-2014-0091, Montreal, Quebec.

[8] Leary, W. M. (2002) *We Freeze to Please: A History of NASA's Icing Research Tunnel and the Quest for Flight Safety*, Tech. rep.

[9] Herman, E. (2006) "Goodrich Icing Wind Tunnel Overview, Improvements and Capabilities," in *44th AIAA Aerospace Sciences Meeting and Exhibit*, AIAA-2006-862, Reno, NV.

[10] Angers, S. (2008) "Chillin' at Work," *Boeing Frontiers*, **vol. 6**(issue 10), pp. 30–31.

[11] AL-KHALIL, K. and L. SALAMON (1998) "Development of the Cox Icing Research Facility," *36th Aerospace Sciences meeting and Exhibit*, (AIAA 98-0097).

[12] PETERSON, A. A. and J. R. OLDENBURG (1990) "Spray Nozzle Investigation for the Improved Helicopter Icing Spray System (IHISS)," in *28th Aerospace Sciences Meeting*, AIAA-90-0666, Reno, NV.

[13] BELL, D. (2003) "Icing at the McKinley Climatic Laboratory," *41st Aerospace Sciences Meeting and Exhibit*, (AIAA-2003-902).

[14] PALACIOS, J. L., E. W. BROUWERS, and E. C. SMITH (2010) "Adverse environment rotor test stand calibration calibration procedures and ice shape correlation," in *American Helicopter Society 66th Annual Forum*, 66-2010-000192, Phoenix, AZ.

[15] KIND, R. J., M. G. POTAPCZUK, A. FEO, C. GOLIA, and A. D. SHAH (1998) "Experimental and Computational Simulation of In-Fight Icing Phenomena," *Progress in Aerospace Sciences*, **34**, pp. 257–345.

[16] RIAHI, M. M. (2007) *Numerical and Experimental Studies of the Mechanical Behaviour at the Ice/Aluminum Interface*, M.s. thesis, University of Quebec.

[17] REICH, A. (1991) "Comparison of rime and glaze deformation and failure properties," in *29th Aerospace Sciences Meeting*, Reno, NV.

[18] CHU, M. L., R. J. SCAVUZZO, and C. J. KELLACKEY (1992) "Tensile properties of impact ices," *30th AIAA Aerospace Science Meeting*, (92-0883).

[19] DRUEZ, J., LAFORTE, and C. J-L TREMBLAY (1989) "Experimental Results on the Tensile Strength of Atmospheric Ice," in *8th Intn. Conference, Offshore Mechanics & Arctic Engng*, Canadian Society for Mechanical Engineering, pp. 59–64.

[20] BROUWERS, E. (2011) "Ice Adhesion Strength Measurements for Rotor Blade Leading Edge Materials," in *American Helicopter Society 67th Annual Forum*, Virginia Beach, VA.

[21] LOUGHBOROUGH, D. and E. HASS (1946) "Reduction of the Adhesion of Ice to De-Icer Surfaces," *Journal of the Aeronautical Sciences*, **13**(3), pp. 126–134.

[22] STALLABRASS, J. and R. PRICE (1962) *On the Adhesion of Ice to Various Materials*, National Research Laboratory, Ottawa.

[23] ITAGAKI, K. (1983) *CRREL Report 83-26, Mechanical Ice Release Processes; I. Self-shedding from high-speed rotors*, *Tech. rep.*, Cold Regions Research and Engineering Laboratory.

[24] Scavuzzo, R. J. and M. L. Chu (1987) *Structural Properties of Impact Ices Accreted on Aircraft Structures*, *Tech. rep.*, NASA Lewis Research Center.

[25] Reich, A. D. (1994) "Interface influences upon ice adhesion to airfoil materials," in *32nd Aerospace Sciences Meeting and Exhibit*, Reno, NV.

[26] Brouwers, E. W., J. L. Palacios, E. C. Smith, A. a. Peterson, B. Rotorcraft, and R. P. Pa (2010) "The Experimental Investigation of a Rotor Hover Icing Model With Shedding," in *The American Helicopter Society 66th Annual Forum*, Phoenix, AZ.

[27] Palacios, J. L. (2008) *Design, Fabrication, and Testing of an Ulotrasonic De-icing System for Helicopter Rotor Blades*, Ph.d. thesis, The Pennsylvania State University.

[28] Buschhorn, S. T., N. Lachman, J. Gavin, and B. L. Wardle (2013) "Electrothermal Icing protection of Aerosurfaces Using Conductive Polymer Nanocomposites," *54th AIAA/ASME/ASCE/AHS/ASC Structures, Structural Dynamics, and Materials Conference, Boston, Massachusetts*, pp. 1–8.

[29] Flemming, R. J. (2003) "A History of Ice Protection System Development at Sikorsky Aircraft," in *FAA In-Flight Icing/Ground De-icing International Conference & Exhibition*, 2003-01-2092, Chicago, Illinois.

[30] Botura, G., D. Sweet, and D. Flosdorf (2005) "Development and Demonstration of Low Power Electrothermal De-icing System," *43rd AIAA Aerospace Sciences Meeting and Exhibit*, (January), pp. 1–15.

[31] Shiping, Z., R. a. Khurram, H. Fouladi, and W. G. Habashi (2012) "Computational Modeling of Ice Cracking and Break-up from Helicopter Blades," in *4th AIAA Atmospheric and Space Environments Conference*, AIAA 2012-2675, New Orleans, Loui, pp. 1–9.

[32] Bain, Jeremy; Cajigas, Juan; Sankar, Lakshmi; Flemming, Robert; Aubert, R. (2010) "Prediction of Rotor Blade Ice Shedding Using Empirical Methods," *2nd AIAA Atmospheric and Space Environments Conference*, (August), pp. 1–14.

[33] Baruzzi, G. S., P. Lagacé, M. S. Aubé, and W. G. Habashi (2007) "Development of a Shed-Ice Trajectory Simulation in FENSAP-ICE," in *SAE Aircraft & Engine Icing International Conference*, 2007-01-3360, Seville, Spain.

[34] Britton, R. K., B. Park, and T. H. Bond (1993) "An Overview of Shed Ice Impact Studies in the NASA Lewis Icing Research Tunnel," in *31st Aerospace Sciences Meeting & Exhibit*, Reno, NV.

[35] DOOGE, D., S. SINGH, K. MASIULANIEC, and K. DEWITT (1993) "Experimental assessment of airframe damage due to impacting ice," in *31st Aerospace Sciences Meeting*, Reno, NV.

[36] TURNS, S. R. (2006) *Thermal-Fluid Sciences: An Integrated Approach*, Cambridge University Press, New York.

[37] WANG, C., J. REDDY, and K. LEE (2000) *Shear Deformable Beams and Plates*, first ed., Elsevier Science, Kidlington, Oxford.